FOI-R--1403--SE
December 2004
ISSN 1650-1942

Scientific report

Jan Burman, Christer Fureby, Leif Persson, Urban Svennberg, Lennart Thaning

Large Eddy Simulation (LES) of Atmospheric Turbulence

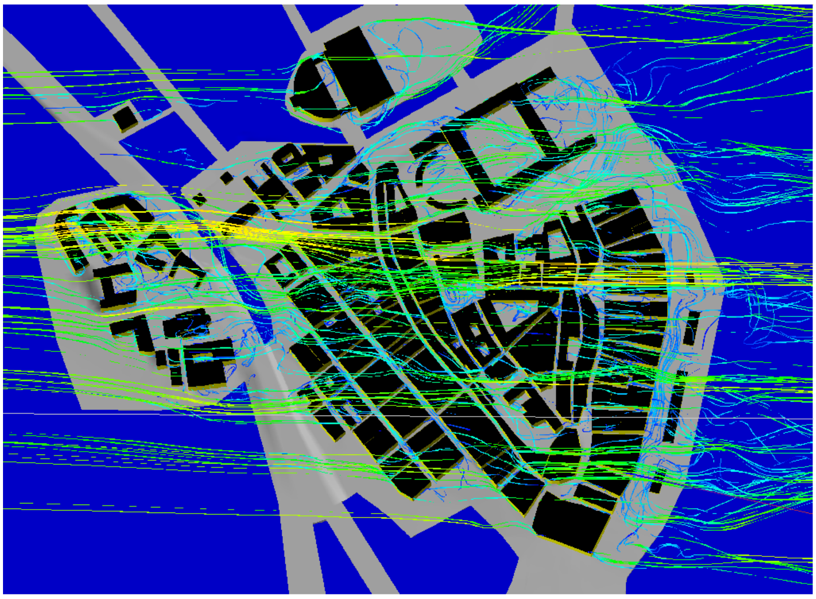

NBC Defence
SE-901 82 Umeå

SWEDISH DEFENCE RESEARCH AGENCY
NBC Defence
SE-901 82 Umeå

FOI-R--1403--SE
December 2004
ISSN 1650-1942

Scientific report

Jan Burman, Christer Fureby, Leif Persson, Urban Svennberg, Lennart Thaning

Large Eddy Simulation (LES) of Atmospheric Turbulence

Issuing organization
FOI – Swedish Defence Research Agency
NBC Defence
SE-901 82 Umeå

Report number, ISRN
FOI-R--1403--SE

Report type
Scientific report

Research area code
39 Interdisciplinary Projects regarding Protection against Weapons of Mass Destruction

Month year
December 2004

Project no.
A4521

Sub area code
39 Interdisciplinary Projects regarding Protection against Weapons of Mass Destruction

Sub area code 2

Author/s (editor/s)
Jan Burman
Christer Fureby
Urban Svennberg
Lennart Thaning
Leif Persson

Project manager
Lennart Thaning

Approved by

Sponsoring agency

Scientifically and technically responsible
Christer Fureby/Lennart Thaning

Report title

Large Eddy Simulation (LES) of Atmospheric Turbulence

Abstract (not more than 200 words)

Large Eddy Simulation has been used to simulate wind and turbulence within complex geometries in the atmosphere. The purpose is to study the possibilities to use LES for simulation of dispersion in urban environment. The LES model is presented with a simulation of channel flow without any obstacles where a number of sub grid models are compared at different Reynolds numbers. Flow around a cube is then presented with comparision of the results from the sub grid models with experimental data. The sub grid model MILES is then selected and used for a simulation of the flow over a geometry derived from Gamla Stan in Stockholm.

Keywords
LES Atmospheric urban turbulence

Further bibliographic information

Language English

ISSN 1650-1942

Pages 40 p.

Price acc. to pricelist

Utgivare
Totalförsvarets Forskningsinstitut – FOI
NBC-skydd
901 82 Umeå

Rapportnummer, ISRN
FOI-R--1403--SE

Klassificering
Vetenskaplig rapport

Forskningsområde
3. Skydd mot NBC och andra farliga ämnen

Månad, år
December 2004

Projektnummer
A4521

Delområde
39 Breda projekt inom skydd mot massförstörelsevapen

Delområde 2

Författare/redaktör
Jan Burman
Christer Fureby
Leif Persson

Urban Svennberg
Lennart Thaning

Projektledare
Lennart Thaning

Godkänd av

Uppdragsgivare/kundbeteckning

Tekniskt och/eller vetenskapligt ansvarig
Christer Fureby/Lennart Thaning

Rapportens titel (i översättning)
Storvirvelsimulering (LES) av turbulens i atmosfären.

Sammanfattning (högst 200 ord)

Storvirvelsimulering (LES) har använts för att simulera vindfält och turbulens för komplexa geometrier i atmosfären. Syftet är att undersöka möjligheten att använda LES för att studera spridning i stadsmiljö. Modellen presenteras med en applikation på enkel kanalströmning utan objekt. Därefter studeras strömning kring en kub och resultatet jämförs med mätningar. Sist presenteras resultatet av en simulering av vindfältet i en geometri hämtad från Gamla Stan i Stockholm.

Nyckelord
LES Atmosfärisk urban turbulens

Övriga bibliografiska uppgifter

Språk Engelska

ISSN 1650-1942

Antal sidor: 40 s.

Distribution enligt missiv

Pris: Enligt prislista

Contents

1. Introduction

With the shift of the perceived nuclear, biological and chemical warfare (NBC) threat from large-scale actions to terrorist actions in urban areas, the demand for detailed simulations of releases and dispersion in complex geometries has attained a much higher priority. Contaminant Transport (CT) analysis treats air- borne pollutants released in industrial accidents, smoke, as well as chemical/biological/radiological agents released in war situations or terrorist attacks. This is now a pressing international problem. A realistic CFD- based plume prediction model of CT in urban areas can be used to address:

- sensor placement and threat analysis;
- contaminant release from targets, e.g., bunkers;
- CT effects on surrounding civilian population, e.g., dosages indoors and outdoors;
- contaminant release from missile intercepts;
- base protection against terrorist attacks, e.g., evacuation, shelter-in-place, and performance degradation;
- education and training of rescue teams and services.
- pyroclastic flows, e.g., visibility;
- in situ mitigation of contaminants, e.g., destroying a contaminant while airborne near the source, and assessing the effectiveness of mitigation strategies;

The combination of very complex geometries with unsteady buoyant and stratified flow physics make whole-domain scalable field studies needed to guide and test model developments complicated and computationally expensive. Simulations of the dispersion of airborne pollutants in urban scale scenarios must predict both the flow conditions as well as the associated behavior of the pollutants, which may be gases, liquids or solids. Relevant physical processes to be modeled include: capturing complex vortex shedding and recirculation behind buildings as well as the associated subgrid scale (SGS) stochastic backscatter; producing a consistent, stratified urban boundary layer; generating realistic wind fluctuations; and additional deposition and resuspension of selected contaminants.

Here is presented an initiative to extend the capabilities and the understanding of the processes that are related to urban dispersion. The results can then be used developing simpler models and templates.

Chapter 2 gives an introduction to CFD in general with a presentation of the numerical model. The ability of the model to handle the increase in complexity from a smooth surface to urban geometry is studied by first evaluating a simulation of a channel flow in chapter 3. A validation study on a surface mounted cube then follows in chapter 4. Finally an application study on flow within an urban geometry is presented in chapter 5.

2. LES model

2.1. Introduction

Computational Fluid Dynamics (CFD) can be viewed as the use of computers to predict fluid flow, in contrast to analytical and experimental methods which also frequently are used to study fluid mechanics. CFD is commonly accomplished by numerical solution of the Navier Stokes Equations (NSE), which are the governing equations of fluid flow, [1]. Numerical solution is the only practical way of solving these equations due to their intrinsic non-linearity and corresponding extensive range of eddy scales. The ratio of the largest eddies (with a size of λ_I) to the smallest Kolmogorov eddies (with size λ_K) can be related to the Reynolds number Re=UL/ν, where U is a characteristic velocity, L a characteristic length and ν the viscosity, i.e. the ratio of inertial to viscous forces, as $\lambda_I/\lambda_K=\mathrm{Re}^{3/4}$. This implies that the degrees of freedom (or number of grid points) required in a Direct Numerical Simulation (DNS), in which all scales are resolved, scale as $\mathrm{Re}^{9/4}$. For high Re-numbers, present-day computers are not powerful enough to handle such problems and therefore alternative methods have to be devised for turbulent flow simulations. However, with the constant improvement in computing power available CFD has been used more and more in research and in industry, to enhance understanding of fluid dynamics and as part of the design process. The sort of simulations which ten years ago would have required an expensive parallel computer or a vector machine can now be carried out on rather inexpensive desktop machines. This increase in available power has lead to an increasing interest in more advanced CFD methods and to the desire to study even more complex problems such as combustion, magneto-hydrodynamics and free surface flows. CFD has already made a profound impact on industrial R&D, in areas such as automotive industry, engine design, ship hydrodynamics and aerospace. However, the ranges of problems that can be solved are limited by the turbulence treatment currently used.

All turbulence modelling methods start by distinguishing between a ‘mean’ component of the flow and a ‘fluctuating’ component which is associated with the turbulence, [2]. In the commonly-used Reynolds Averaged Navier Stokes (RANS) methods, [3], the starting point is an ensemble average of the flow (sometimes time-averaging or averaging over homogeneous directions are used instead) to generate the RANS equations. These are then explicitly solved, together with models for the fluctuating, turbulent component. In Large Eddy Simulation (LES) methods, [4-7], an explicit or implicit spatial filtering operation is applied to separate the large-scale resolvable flow component (corresponding to the ‘mean’ component) and the small-scale component. Applying this filtering operation to the NSE provides a set of equations of the large scale flow, together with small scale components which effects on the large scale flow has to be modelled separately. Since the width of the filter is usually based on the computational grid spacing, the components are referred to as Grid Scale (GS) and Sub Grid Scale (SGS) components. Splitting the flow in this way based on a length scale means that some parts of the turbulence – the large eddies – are being simulated explicitly. Since turbulence is a stochastic, or almost stochastic, process, this means that the simulation must be time-dependent, and since turbulence is inherently three-dimensional, the simulation must also be three-dimensional. For turbulent flows where the mean flow is stationary or two-dimensional, RANS methods are considerably cheaper. However, many important and interesting flows do not fall into any of these categories in which case LES become competitive. LES hold the promise of providing more information about the flow, since LES inherently simulates the dynamics of the large-scale flow, including parts of the intermediate scale turbulence. LES is also potentially more accurate, [7] since the LES-equations being solved are closer in form to the NSE, which they reduce to when the mesh is refined, which is not the case for RANS, [8]. LES methods as applied to simple flows are now fairly well understood – to quote Spalart: “Away from boundaries and without chemistry, Large Eddy Simulation (LES) appears well understood, and in the authors opinion there is little to gain by refining the SGS model (Fureby et al 1997)”, [9]. The boundaries, however, themselves remain a stumbling block, [10].

2.2. Large Eddy Simulation Models

Here we outline the classical LES formulation, give a few examples of alternative formulations and finish with a discussion of the near-wall complication.

2.2.1. Mathematical Formulation

In LES the flow variables are decomposed into large- scale components (denoted by overbars) and small-scale (subgrid) components (denoted by primes) by applying a filtering[1] operation,

$$\bar{f}(\mathbf{x},t)=G*f(\mathbf{x},t)=\int_D G(\mathbf{x}-\mathbf{z},\Delta)f(\mathbf{z},t)d^3\mathbf{z}, \tag{1}$$

where G is the filter function and Δ the filter width. Applying the filtering operation to the NSE yields,

$$\begin{cases}\nabla\cdot\bar{\mathbf{v}}=m^{\rho}, \\ \partial_t(\bar{\mathbf{v}})+\nabla\cdot(\bar{\mathbf{v}}\otimes\bar{\mathbf{v}})=-\nabla\bar{p}+\nabla\cdot\bar{\mathbf{S}}-\nabla\cdot\mathbf{B}+\mathbf{m}^{v},\end{cases} \tag{2}$$

where $\bar{\mathbf{v}}$ is the velocity, $\bar{p}$ the pressure, $\bar{\mathbf{S}}=2\nu\bar{\mathbf{D}}$ the viscous stress tensor, $\bar{\mathbf{D}}=\frac{1}{2}(\bar{\mathbf{L}}+\bar{\mathbf{L}}^T)$ the rate-of-strain tensor, $\bar{\mathbf{L}}=\nabla\bar{\mathbf{v}}$ the velocity gradient tensor, and ν the viscosity. Specific to the LES model (2) are the subgrid stress tensor $\mathbf{B}=\overline{\mathbf{v}\otimes\mathbf{v}}-\bar{\mathbf{v}}\otimes\bar{\mathbf{v}}$ and the commutation errors are $m^{\rho}=[G*,\nabla]\mathbf{v}$ and $\mathbf{m}^{v}=[G*,\nabla](\mathbf{v}\otimes\mathbf{v}+p\mathbf{I}-\mathbf{S})$, where $[G*,\nabla]f=\overline{\nabla f}-\nabla\bar{f}$ is the commutation operator, [12-13]. Only the resolved scales are thus retained in LES whereas the subgrid scale flow physics is grouped into B, which has to be modelled using a functional expression of the type $\mathbf{B}(\mathbf{x},t)=\mathbf{B}[\bar{\mathbf{v}}(\mathbf{x}',t');\mathbf{x},t]$. Physical arguments and mathematical analysis, e.g. [13-15], suggest that: (i) B is invariant under a change of frame; (ii) B is positive definite symmetric, provided that $G(x,\Delta)$ is symmetric; and (iii) that the inequalities $k=\frac{1}{2}tr\mathbf{B}\geq 0$, $k^2\geq\|\mathbf{B}\|^2$ and $\det\mathbf{B}\geq 0$ must be satisfied for B to be positive definite. Furthermore, the commutation error terms, m^{ρ} and m^{v}, reflect the fact that filtering and differentiation do not generally commute, [13, 16]. The effects of m^{ρ} and m^{v} on the resolved flow are not yet fully understood and must be further examined, [16], and in the meantime, these terms are usually grouped into the subgrid stress tensor B that is subject to modelling.

2.2.2. Subgrid Modelling

We usually separate between *Functional modelling*, which consists of modelling the action of the subgrid scales on the resolved scales, and *Structural modelling*, which consists of modelling the subgrid stresses without incorporating any knowledge about the interactions between the subgrid and the resolved scales, [6]. However, for the purpose of this paper we prefer to instead separate between *isotropic* and *anisotropic* subgrid models since high Re-number complex flows often are characterized by anisotropic flow on a wide range of scales – typically reaching into the range of scales that require modelling, as e.g. in the near-wall region. The most frequently used subgrid models belong to the first category, viz.,

$$\mathbf{B}_D=\mathbf{B}-\tfrac{2}{3}k\mathbf{I}=-2\nu_k\bar{\mathbf{D}},\quad k=\tfrac{1}{2}tr\mathbf{B}, \tag{3}$$

---

[1] The filtering function is an operator that returns the filtered field and additionally sub grid scale terms that needs to be modelled as they are unknown quantities.

where ν_k is the (scalar) subgrid eddy-viscosity. To close (3) we need models for the eddy-viscosity ν_k and the turbulent kinetic energy k, and for this we assume the existence of typical length and velocity scales and we infer separation between resolved and subgrid scales. Among these we have the One-Equation-Eddy-Viscosity Model (OEEVM), [17],

$$\begin{aligned}&\partial_t(k)+\nabla\cdot(k\mathbf{v})=2\nu_k\|\bar{\mathbf{D}}\|^2+\nabla\cdot((\nu+\nu_k)\nabla k)+c_\varepsilon \tfrac{k^{3/2}}{\Delta},\\&\nu_k=c_k\Delta k^{1/2},\end{aligned} \tag{4}$$

and the Smagorinsky (SMG) model, [18],

$$k=c_I\Delta^2\|\bar{\mathbf{D}}\|^2,\ \ \nu_k=c_D\Delta^2\|\bar{\mathbf{D}}\|, \tag{5}$$

where the model coefficients (c_I, c_D, c_k and $c_{\square}$) are evaluated either from a $|k|^{-5/3}$ inertial sub-range behavior resulting in constant coefficients, or from a dynamic procedure, producing spatio-temporally varying coefficients. Different dynamic calculation methods have been suggested, such as the dynamic Smagorinsky Model (DSMG), [19], the One-Equation Dynamic Localization Model, (DLM), [20], the Localized Dynamic Kinetic Energy Model (LDKM), [21-23], as well as the Lagrangian Dynamic Model (LDM), [24].

For anisotropic flows, with anisotropy extending into the range of subgrid scales, more advanced subgrid models are required. Structural models are superior (at least from a theoretical standpoint) to functional models in such flows since they do not rely on the local isotropy assumptions on which the functional models are based. Among the best examples of structural models are the Mixed Model (MM) of Bardina *et al.*, [25],

$$\mathbf{B}=\overline{\bar{\mathbf{v}}\otimes\bar{\mathbf{v}}}-\bar{\bar{\mathbf{v}}}\otimes\bar{\bar{\mathbf{v}}}-2\nu_k\bar{\mathbf{D}}, \tag{6}$$

and the Differential Stress Equation Model (DSEM), Deardorff, [26]. The DSEM uses a modelled transport equation for the subgrid stress tensor B,

$$\partial_t(\mathbf{B})+\nabla\cdot(\mathbf{B}\otimes\bar{\mathbf{v}})=-(\bar{\mathbf{L}}\mathbf{B}^T+\mathbf{B}\bar{\mathbf{L}}^T)+\nabla\cdot(\nu_k\nabla\mathbf{B})-c_m\tfrac{k^{1/2}}{\Delta}\mathbf{B}_D+\tfrac{2}{5}k\bar{\mathbf{D}}_D+(\tfrac{2}{3}c_m-c_\varepsilon)\tfrac{k^{3/2}}{\Delta}\mathbf{I}, \tag{7}$$

where $\nu_k=c_k\Delta k^{1/2}$ and $k=\frac{1}{2}\mathrm{tr}\mathbf{B}$. The model coefficients are estimated from isotropic turbulence, and take the values c_m=4.13, c_k=0.07 and c_ε=1.35. Anisotropic functional models have been developed by Carati & Cabot, [27], and Abba *et al.*, [28], using fourth-rank tensor eddy-viscosities, by Horiuti, [29], using multi-level filtering, and by Schumann, [17], and Sullivan *et al*, [30], using a decomposition of **B** into isotropic and anisotropic components.

2.2.3. Near-Wall Flow Physics and Modelling

Close to a solid wall, to the leading order in y, being the distance from the wall, the resolvable velocity $\bar{\mathbf{v}}$ can be expanded in a Taylor series of the form,

$$\bar{\mathbf{v}}=(\bar{b}_1y)\mathbf{e}_1+(\bar{c}_2y^2)\mathbf{e}_2+(\bar{b}_3y)\mathbf{e}_3, \tag{8}$$

where e_i, $i=1,2,3$, are unit vectors in the streamwise, wall-normal and spanwise directions, and b_1, c_2 and b_3 are random functions. Similarly for B_{ij},

$$B_{ij}=\begin{bmatrix} (\overline{b_1^2}-\bar{b}_1^{\,2})y^2 & (\overline{b_1c_2}-\bar{b}_1\bar{c}_2)y^3 & (\overline{b_3c_2}-\bar{b}_3\bar{c}_2)y^2 \\ & (\overline{c_2^2}-\bar{c}_2^{\,2})y^4 & (\overline{b_3c_2}-\bar{b}_3\bar{c}_2)y^3 \\ sym & & (\overline{b_3^2}-\bar{b}_3^{\,2})y^2 \end{bmatrix} \tag{9}$$

The LES model is thus required to satisfy not only the boundary condition $\bar{\mathbf{v}}=\mathbf{0}$ but also the conditions (9) on B when $y\to0$. Considering the SMG model, (3)-(5), we have that $\partial\bar{v}_1/\partial x_2=\bar{b}_1$ and $\partial\bar{v}_3/\partial x_2=\bar{b}_3$ so that $B_{12}=-c_D\Delta^2(\bar{b}_1^2+\bar{b}_3^2)^{1/2}\bar{b}_1$ and unless $\Delta\propto y^{3/2}$ incorrect asymptotic behaviour at the wall is obtained. For example, if (3) is to be used, a necessary requirement is that $k\propto y^2$ and $\nu_k\propto y^3$, when $y\to0$, in order for B to comply with (9). Most structural models satisfy (9) automatically but many models must be modified to satisfy (9). This can be done using:

Damping functions, D, that act as regularization prefactors to ν_k, such that $\nu_k=D\nu_k$. Typically $D=(1-\exp(-(\beta y^+)^3))^{1/2}$, where $y^+=u_\tau y/\nu$ is the viscous length scale, $u_\tau=\tau_w^{1/2}$ the friction velocity, τ_w the wall shear stress and $\bar{v}_i^+=\bar{v}_i/u_\tau$ a non-dimensionalized velocity component;

Dynamic modelling based on Germanos identity, $\mathbf{L}=\mathbf{T}-\tilde{\mathbf{B}}$, [19-20], in which $\mathbf{L}=\overline{\bar{\mathbf{v}}\otimes\bar{\mathbf{v}}}-\bar{\bar{\mathbf{v}}}\otimes\bar{\bar{\mathbf{v}}}$ and $\mathbf{T}=\overline{\mathbf{v}\otimes\mathbf{v}}-\bar{\bar{\mathbf{v}}}\otimes\bar{\bar{\mathbf{v}}}$. By assuming that B and T can be closed with models of the same functional form i.e. $\mathbf{B}=-2c_D\Delta^2\|\bar{\mathbf{D}}\|\bar{\mathbf{D}}$ and $\mathbf{T}=-2c_D\bar{\Delta}^2\|\bar{\bar{\mathbf{D}}}\|\bar{\bar{\mathbf{D}}}$ we now have that $\mathbf{L}_D=c_D\mathbf{X}-\overline{c_D\mathbf{Y}}$, where $\mathbf{X}=-2\Delta^2\|\bar{\mathbf{D}}\|\bar{\mathbf{D}}$ and $\mathbf{Y}=-2\bar{\Delta}^2\|\bar{\bar{\mathbf{D}}}\|\bar{\bar{\mathbf{D}}}$, respectively. Hence, in the least-squares sence we have $c_D=\mathbf{M}\cdot\mathbf{L}/\mathbf{M}\cdot\mathbf{M}$, where $\mathbf{M}=\mathbf{X}-\bar{\mathbf{Y}}$.

Dynamic modelling based on the self-similarity between B and $\mathbf{L}=\overline{\bar{\mathbf{v}}\otimes\bar{\mathbf{v}}}-\bar{\bar{\mathbf{v}}}\otimes\bar{\bar{\mathbf{v}}}$, [21-23]. This may be used to evaluate the coefficient c_k and c_ε in the OEEVM (4). Bounds for c_k and c_ε are determined from the realizabilty constraints.

Models for the eddy-viscosity coefficients that include viscous effects, cf. [31]. If the model coefficients (c_D and c_k) are derived from more elaborate versions of the energy spectrum than the inertial subrange spectrum $E=K_0\varepsilon^{2/3}|\mathbf{k}|^{-5/3}$, e.g. the Pao spectrum $E=\exp(-\tfrac{3}{2}K_0(|\mathbf{k}|\lambda_K)^{4/3})$, it is found that these coefficients are not constants but complicated functions of the mesh Re-number $Re_\Delta=\Delta^2\|\bar{\mathbf{D}}\|/\nu$. This can be interpreted as models with scale-dependent coefficients and improves the predictive capabilities for transitional and wall-bounded flows.

Alternatively we may use wall models. The simplest wall models are based on analytical expressions for the wall shear stress, τ_w, and they provide an algebraic relationship between the local wall stresses and the tangential velocities at the first off-wall nodes. Such algebraic models all imply the logarithmic law of the wall for the mean velocity, which is not generally valid in complex flows. The equations governing for the wall-layer can be approximated by,

$$\partial_y(\nu(\partial_y\bar{v}_i)-B_{iy})=g_i;\;\; g_i=\partial_i\bar{p}+\partial_t\bar{v}_i+\partial_j(\bar{v}_i\bar{v}_j)-f_i, \tag{10}$$

[4]. Assuming that $g_i=0$ the stress $\nu(\partial_y\bar{v}_i)-B_{i2}$ is independent of y, and since $B_{iy}=0$ on the wall (10) can be integrated analytically to give the law-of-the-wall,

$$\bar{v}^+=\begin{cases} y^+ & \text{if } y^+\le y_0^+, \\ \tfrac{1}{\kappa}\ln|y^+|+B & \text{if } y^+>y_0^+, \end{cases} \quad y_0^+\approx11.225, \tag{11}$$

where $\kappa \approx 0.41$ is the von-Karmán constant and $B \approx 5.2$. If $g_i = \partial_i \bar{p}$ it is still possible to integrate (10) analytically to recover the modified law-of-the-wall,

$$\bar{v}^+ = \begin{cases} y^+ + \frac{y^+}{2u_\tau^2} \partial_i \bar{p} & \text{if } y^+ \le y_0^+(u_\tau, \partial_i \bar{p}), \\ \frac{1}{\kappa} \ln|y^+| + \frac{y^+}{\kappa u_\tau^2} \partial_i \bar{p} + B & \text{if } y^+ > y_0^+(u_\tau, \partial_i \bar{p}). \end{cases} \tag{12}$$

For the full case, $g_i = \partial_i \bar{p} + \partial_t \bar{v}_i + \partial_j (\bar{v}_i \bar{v}_j) - f_i$, equation (10) has to be solved numerically. This approach has successfully been used by Wang, [32] and by Wang & Moin, [33], in which (10) is solved on an embedded near-wall grid to determine τ_w, using a mixing length model. Alternatively, (11) or (12) can be used to modify the subgrid model by adding a subgrid wall-viscosity ν_{BC} to the viscosity ν on the wall so that the effective viscosity, $\nu + \nu_{BC}$, becomes,

$$\nu + \nu_{BC} = \tau_w / (\partial v_y / \partial y)_P = u_\tau y_{y,P} / v_{y,P}^+, \tag{13}$$

where the superscript P denotes that the quantity is to be evaluated at the first grid point away from the wall. This model can, in principle, be combined with any other subgrid model, and in the notation +WM is added to the baseline subgrid model name.

2.2.4. Monotone Integrated LES

In Monotone Integrated LES (MILES) the discretization effectively filters the NSE across the grid using an anisotropic kernel. When founding MILES on concepts like the Flux Corrected Transport (FCT), [35], the functional reconstruction of the convective fluxes is done using a flux-limiting method combining a high-order flux-function with a low-order dispersion-free flux-function using a non-linear flux-limiter Γ. Moreover, the functional reconstruction of the viscous fluxes is typically performed using linear interpolation. Similar approaches have been used by several other authors, [36-40], and are discussed in greater detail in [10], and references therein. Physical considerations motivating MILES have been presented in [40], and some formal properties were recently documented using databases of free and wall-bounded flows, [41]. The modified equations provide the most suitable platform for comparing MILES and LES and following Fureby & Grinstein, [40], the implicit subgrid model is,

$$\mathbf{B} = \mathbf{C}(\nabla \mathbf{v})^T + (\nabla \mathbf{v})\mathbf{C}^T + \beta^2 (\nabla \mathbf{v})\mathbf{d} \otimes (\nabla \mathbf{v})\mathbf{d}, \quad \mathbf{C} = \beta(\mathbf{v} \otimes \mathbf{d}), \tag{14}$$

where $\mathbf{d}$ is the inter-cell distance and $\beta = \beta(\Gamma)$. Because of the tensorial nature of the subgrid viscosity MILES offers an attractive alternative to conventional subgrid models when seeking improved LES for inhomogeneous flows.

2.3. Numerics

The application of LES to engineering problems requires not only good subgrid models and fast computers, but also accurate and robust numerical methods. Unstructured grids are desirable since the time required for generating unstructured grids is usually considerably lower than for block-structured grids. To this end the Finite Volume (FV) method is appropriate. However, non-dissipative schemes that conserve not only momentum but also kinetic energy are required for successful LES computations. Discrete conservation of kinetic energy ensures robustness without numerical dissipation, which compromises accuracy.

In the FV-method, the domain D is partitioned into non-overlapping cells Ω_P. The cell-average of the field f over the Pth cell is $f_P=\frac{1}{\delta V}\int_\Omega f dV$ so that Gauss theorem may be used to formulate the semi-discretized LES-equations. By integrating these in time, using e.g. a multi-step method, [42], the discretized LES-equations (i.e. equations (2) and (18)) become,

$$\begin{cases} \frac{\beta_i \Delta t}{\delta V_P}\sum_f [F_f^{C,\rho}]^{n+i}=0, \\ \sum_{i=0}^{m}(\alpha_i(\bar{\mathbf{v}})_P^{n+i}+\frac{\beta_i \Delta t}{\delta V_P}\sum_f[\mathbf{F}_f^{C,v}+\mathbf{F}_f^{D,v}]^{n+i})=-\beta_i(\nabla\bar{p})_P^{n+i}\Delta t+\beta_i\bar{\mathbf{f}}_P^{n+i}\Delta t, \end{cases} \tag{15}$$

where m, α_i and β_i are parameters of the scheme, whereas $\mathbf{F}_f^{C,v}=(\bar{\mathbf{v}}\cdot d\mathbf{A})_f\bar{\mathbf{v}}_f$, $F_f^{C,\rho}=(\bar{\mathbf{v}}\cdot d\mathbf{A})_f$ and $\mathbf{F}_f^{D,v}=(\nu\nabla\bar{\mathbf{v}}-\mathbf{B})_f d\mathbf{A}$ are the convective and viscous fluxes. In order to obtain 2nd order accuracy, a cell-centered scheme is used, utilizing linear interpolation for the convective fluxes and central difference approximations for the gradients in the viscous fluxes. Conservation of kinetic energy is automatically satisfied. Time-integration is carried out by a three-point scheme defined by $m=2$, $\alpha_0=1/2$, $\alpha_1=-2$, $\alpha_2=3/2$, $\beta_0=\beta_1=0$ and $\beta_2=1$, and hence,

$$\begin{cases} a_P(\bar{\mathbf{v}})_P^{n+2}=\mathbf{H}(\bar{\mathbf{v}})-(\nabla\bar{p})_P^{n+2}+(\bar{\mathbf{f}})_P^{n+2}, \\ \mathbf{H}(\bar{\mathbf{v}})=\sum_N a_N(\bar{\mathbf{v}})_N^{n+2}+\frac{1}{2\Delta t}(\bar{\mathbf{v}})_P^{n}-\frac{2}{\Delta t}(\bar{\mathbf{v}})_P^{n+1}, \end{cases} \tag{16}$$

where the coefficients a_P and a_N are functions of the dependent variables. By combining (15_1) and (15_2), we obtain the Poisson equation,

$$\nabla\cdot(a_P^{-1}(\nabla\bar{p})^{n+2})=\sum_f(a_P^{-1}[\mathbf{H}(\bar{\mathbf{v}})+(\bar{\mathbf{f}})_P^{n+2}])_f\cdot d\mathbf{A} \tag{17}$$

where the Laplace operator is discretized in a standard manner and $F_f^{C,\rho}$ is evaluated from the interpolated velocity field $\bar{\mathbf{v}}_f^{n+2}=(a_P^{-1}[H(\bar{\mathbf{v}})-(\nabla\bar{p})_P^{n+2}+\bar{\mathbf{f}}_P^{n+2}])_f$. The scalar equations are usually solved sequentially, with iteration over the explicit source terms to obtain rapid convergence, with the additional requirement that the Courant number $Co<0.4$.

While tetrahedral cells allow complex geometries to be easily meshed, they are not well suited for turbulent flows – our experience shows that hexahedral cells are preferable since they give more accurate solutions. The grid may hence be a combination of arbitrary polyhedral cells, with mainly hexahedral cells but using e.g. tetrahedral cells in regions that are difficult to mesh with ordinary hexahedral cells.

3. Flow without any blocking obstacles

3.1. Fully Developed Turbulent Channel Flow

The first test case to be discussed is a fully developed turbulent channel flow at (bulk-) Re-numbers between 15,000 and 800,000. The channel is confined between two perfectly smooth parallel plates 2h apart, where h is the channel half-width. The flow is driven by a fixed mass flow in the streamwise (e_x) direction defining the mean velocity $\langle\bar{\mathbf{v}}\rangle$. No-slip conditions are used in the cross-stream (e_y) direction and periodic conditions are used in the spanwise (e_z) direction. As initial conditions a parabolic velocity distribution is used. After reaching a statistically steady state the runs were continued for another $40\cdot h/u_\tau$ time-units to collect appropriate statistics. The friction velocity is $u_\tau=\tau_w^{1/2}$ and τ_w is the wall-shear stress. The size of the channel is 6h×2h×3h in the streamwise, cross-stream and spanwise directions, respectively.

Instead of varying the grid we vary the mass flow to obtain three target Re-numbers: Re_τ=395, 2030 and 10,000, of which the first correspond to the DNS data, [43-44], and the second to the experimental data, [45]. The grid consists of 60^3 cells with uniform spacing in the stream- and spanwise directions whereas geometrical progression is used in the e_y direction to cluster the grid towards the walls. Runs and nominal parameters are collected in Tables 1 and 2, respectively.

Table 1. Channel flow grids.

Re	Δx_1^+	$\min(\Delta x_2^+)$	Δx_3^+
395	40	0.3	20
2030	200	2	100
10,000	1000	11	500

Table 2. Nominal parameters of the channel flow runs

Run	Re	Grid	Subgrid model	C_f
Dean [53]	395		—	0.00655
I	403	60^3	OEEVM	0.00648
II	402		OEEVM+WM	0.00653
III	399		LDKM	0.00654
IV	405		MILES	0.0065
V	404		DES	0.0061
VI	404		HOM	0.00647
Dean [53]	2030			0.00435
VII	2036	60^3	OEEVM	0.00421
VIII	2046		OEEVM+WM	0.00439
IX	2049		LDKM	0.00436
X	2021		MILES	0.0433
XI	2054		DES	0.0423
Dean [53]	10000			0.00253
XII	10087	60^3	OEEVM	0.00212
XIII	10076		OEEVM+WM	0.00238
XIV	10054		LDKM	0.00244
XV	10065		MILES	0.00259
XVI	10034		DES	0.00261

In Figure 1 are shown the main flow features of the channel flow in terms of vortex lines, contours of $\langle \bar{v}_x \rangle$ and iso-surfaces of the second invariant of the velocity gradient $Q=\frac{1}{2}(\|\mathbf{W}\|^2-\|\mathbf{D}\|^2)$. The location of a vortex line is given by the equation $d\mathbf{x}/ds=\omega|/|\bar{\omega}|$, where s is the distance along the vortex line. This equation is integrated using a 3rd order Runge-Kutta method together with a 2nd order linear interpolation scheme to compute $\bar{\omega}$ from the grid points. By correlating iso-surfaces of Q with $\bar{\mathbf{v}}$ close to the wall it is found that vortices above the low-speed streaks are often ejected away from the wall, as found in experiments and LES and DNS, producing hairpin vortices stretched by the ambient shear. By this mechanism vorticity produced in the viscous region is advected into the boundary layer, making it turbulent. As in DNS and other LES the hairpin vortices are often asymmetric – with one leg stronger than the other. The spanwise resolution is found more important for the accurate prediction of the coherent structure dynamics than the streamwise resolution. The wall-normal resolution is critical for the correct prediction of τ_w, which, in turn, is important for making correct estimates of the drag.

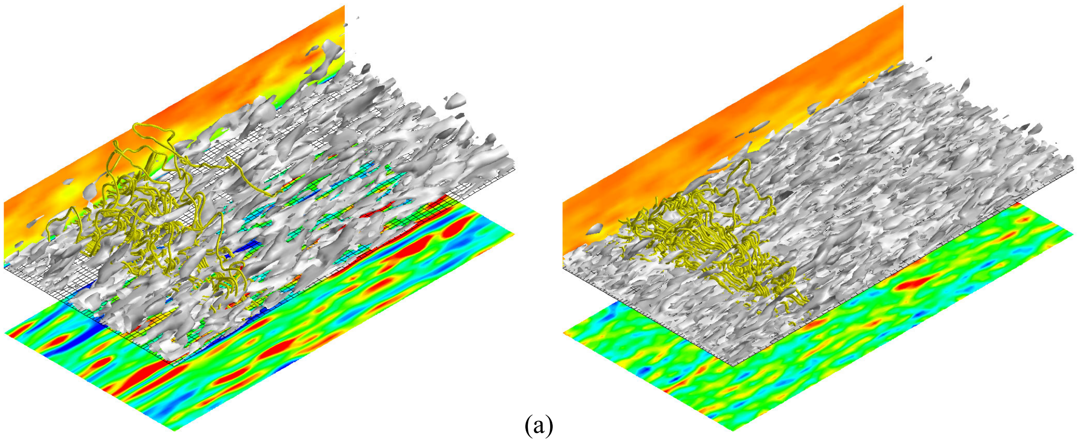
(a) (b)

Figure 1. Perspectives of fully developed turbulent channel flow simulations at (a) Re_τ=395 and (b) Re_τ=10000. Both datasets presented are obtained with the LDKM.

In Figure 2 we compare our LES predictions of the time-averaged streamwise velocity $\langle \bar{v}_x \rangle$ (integrated over x and z) with the DNS data, [45], experimental data, [45], and analytical expressions. In Figure 2a we plot $\langle \bar{v}_x \rangle / u_\tau$ against y/h from the wall, whereas in Figure 2b we plot $\langle \bar{v}_x \rangle / u_\tau$ against $y^+ = yu_\tau/\nu$. For R_τ=395 all LES models examined (cf. Table 2) show excellent agreement with the DNS data across the entire channel. The integrated difference along the cross-stream coordinate, y, is smaller than 2% of the bulk velocity for any model. Hence, when the flow is very well resolved the details of the subgrid model are of little importance to the resolved flow, since most of the energy (about 98%) and structures are resolved on the grid. For R_τ=2030 we still see good agreement between LES and experimental data, but with somewhat larger scatter in the LES data. This case is reasonably well resolved, with about 90% of the energy belonging to the resolved scales. For R_τ=10,000 we do not have any data to compare with, but we may compare (asymptotically) with the lower Re_τ-number velocity profiles and the log-law. The scatter among the LES models is now larger, and we find the best agreement between the log-law and the LES results for DES,(see [10], and references therein), and LDKM followed, in turn, by MILES, OEEVM+WM and OEEVM. The DES model is successful since the Spalart-Allmares model works for zero pressure-gradient boundary-layers, [34]. The LDKM is successful since ν_k responds to the accumulation of energy in the small scales by adjusting the dissipation before it contaminates the resolved scales. MILES performs since it mimics the anisotropies of the resolved flow, [40]. OEEVM+WM works since the channel flow is dominated by two boundary layers, for which the wall model is tailor-made, but the OEEVM appears unable to capture the near-wall boundary layer very well.

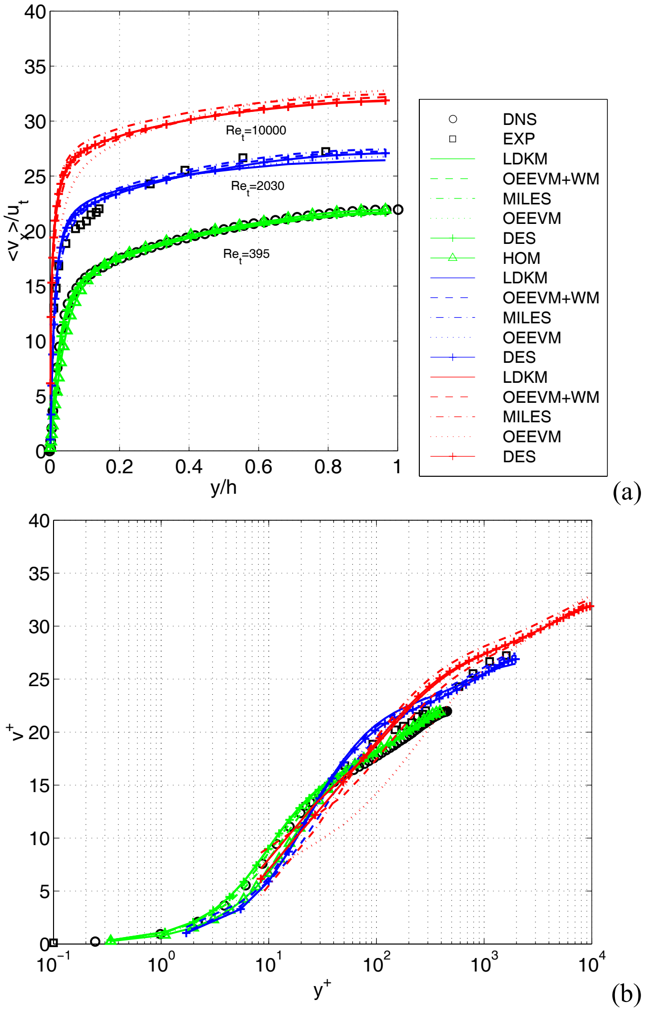

Figure 2. Time-averaged streamwise velocity profiles. (a) in linear scaling and (b) in logarithmic scaling for fully developed turbulent channel flows at Re_τ=395, 2030 and 10,000.

In Figure 3 we compare LES predictions of the resolved kinetic energy $k=\frac{1}{2}\langle \bar{v}_i'^2 \rangle$, where $\bar{\mathbf{v}}'=\bar{\mathbf{v}}-\langle \bar{\mathbf{v}} \rangle$ are the velocity fluctuations, (integrated over x and z) with experimental data, [48], DNS data, [45]. For R_τ=395 very good agreement with the DNS results is obtained across the entire channel for any LES model. For R_τ=2030 the agreement between LES and data is only fair; best agreement is obtained with the LDKM and worst agreement is obtained with the DES model. The trend is that the predicted profiles are wider than the measured profiles, and that the LES models cannot capture the peak in k, at about $y^+\approx 15$, but overpredicts it by about 15%. For R_τ=10,000 the scatter between the LES predictions is wider.

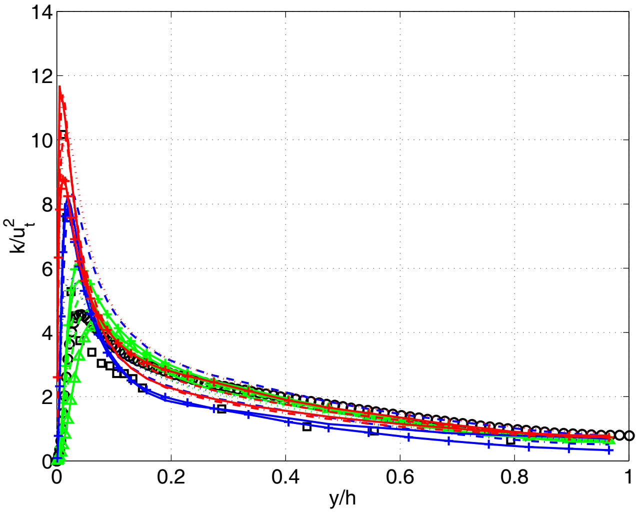

Figure 3. Turbulent kinetic energy, k, profiles for fully developed turbulent channel flows at Re_τ=395, 2030 and 10,000.

In Figure 4 we compare LES predictions of the resolvable shear stress $\bar{R}_{xy}=\langle \bar{v}'_x \bar{v}'_y \rangle$, with experimental data, [43], and DNS data, [45], for the total shear stress $R_{xy}=\langle v'_x v'_y \rangle$. Both R_{xy}-profiles are bounded by $R_{xy}=u_\tau^2 y/h$, which constitute an upper bound for R_{xy}. For R_τ=395 excellent agreement with the DNS results is obtained between 0.3<y/h<1, and between 0<y/h<0.3 $\bar{R}_{xy}<R_{xy}$, as a consequence of the action of the subgrid model, that covers almost 80% of this difference. For R_τ= 2030 and R_τ=10,000 similar results are observed, but since R_{xy} is expected to follow $R_{xy}=u_\tau^2 y/h$ asymptotically with increasing Re_τ-number, the fraction of R_{xy} to be covered by the subgrid model is increasing, thus putting larger demands on the subgrid model. The only exception from the general behaviour is the DES model, which however gives good predictions for other quantities examined. At present we do not know the cause of these anomalities.

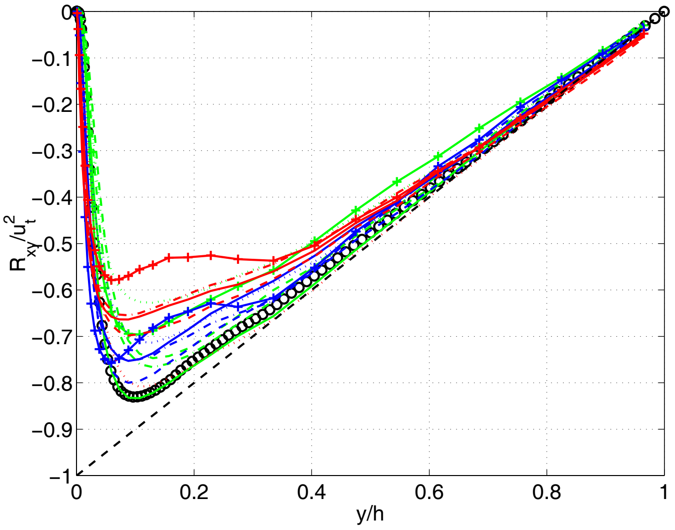

Figure 4. Reynolds shear stress, R_{xy}, profiles for fully developed turbulent channel flows at Re_τ=395, 2030 and 10,000.

3.2. Conclusions

Comparing statistics from the LES with the correlations of Dean, [48], $U_C/U_m \approx 1.28 \cdot \mathrm{Re}_m^{-0.016}$ and $C_f \approx 0.073 \cdot \mathrm{Re}_m^{-0.25}$, where U_C is the mean centerline velocity and $\mathrm{Re}_m = U_m 2\delta/\nu$, shows good agreement at $\mathrm{Re}_\tau=395$, but at $\mathrm{Re}_\tau=2030$ and 10,000 this agreement declines. In general, however LDKM, DES and MILES give best agreement. This is related to the resolution; at $\mathrm{Re}_\tau=395$ the mean streak-spacing is well-resolved, whereas for the remaining Re_τ it is not. For $\mathrm{Re}_\tau=2030$ and 10,000 the mean streak-spacing seems to be related to the spanwise resolution.

4. The Flow around a Surface Mounted Cube

4.1 Introduction

To validate LES algorithms used for simulation of atmospheric flow and dispersion, at least partially, we should make a comparison with laboratory experiments. To validate the flow model, we have chosen the Martinuzzi and Tropea experiment on a surface mounted cube in a channel [50]. We start, however, with a short review of results on the flow around surface mounted cubic obstacles.

4.2 Review of some earlier results.

Early experimental results are presented in [48], where two cases are considered. The first one is a uniform (except for a boundary layer with height much smaller than the cube height) laminar upstream flow, and the second one is a sheared turbulent upstream flow (a simulated atmospheric boundary layer). In both cases there are separating shear layers at the leading edges of the cube. In the laminar case it was observed that with increasing Reynolds number (based on the cube height and the free stream velocity), the shear layer separating from the top of the cube moved upwards, caused by the transition point moving closer to the leading edge. Beyond a Reynolds number 30 000 the shear layer appeared to be turbulent from the leading edge, and no further variations occurred beyond that value.

The main observation of [48] was that compared to the laminar case, in the turbulent case the separating shear layers reattach to the body surface (probably intermittently), and that the size of the wake is significantly reduced. Hence, to predict the extent of the wake it is important to have both an accurate upstream mean velocity profile and accurate description of the upstream turbulence.

In [49], the flow pattern around a surface mounted cube is investigated, based on oil—film visualization experiments and topological considerations, assuming that the average velocity field is continuous. This flow pattern is confirmed in [50] where more detailed measurements are presented.

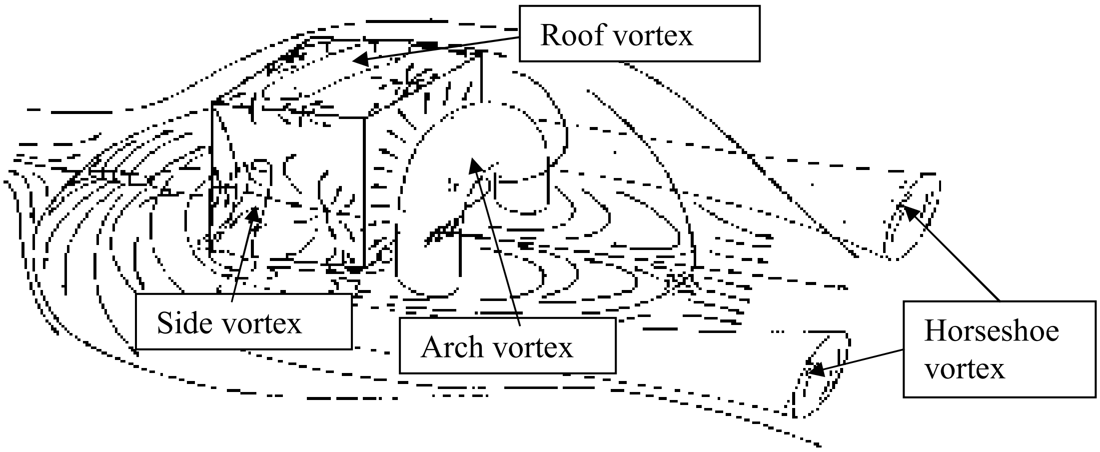

Figure 5. Average velocity streamline pattern for flow around surface mounted cube, from Martinuzzi and Tropea [50], reproduced by permission. The main vortex structures are seen in this Figure, the horseshoe vortex, the lateral side and roof vortices and the arch vortex behind the cube. The arch vortex, however, is an artifact of the averaging and not clearly seen in the instantaneous flow.

The main observed phenomena are the following: streamwise vortices are generated within the shear layer upstream of the cube, and affect the flow near the obstacle, reorganizing the recirculation region and influencing the downstream recovery region. The main vortex structures are: the horseshoe vortex, the wake vortex and lateral vortices on the top and lateral sides of the cube. The horseshoe vortex system is in the region upstream the wall—obstacle junction, is extending over the whole width of the obstacle and deflected downstream. Vertical vortices behind the cube entrain the surrounding fluid and convect it along the plane of symmetry. Exchange of flow between the separation regions is found, confirming the results of Hunt et al.[49], that there are no closed separation bubbles. However, it must be emphasized that, as is pointed out in [51], the flow is highly intermittent, especially between the main upstream separation line and the time averaged location of the center of the horseshoe vortex. Hence the features of the mean flow need not always be present in the instantaneous flow field. For example the arch vortex behind the cube is an effect of a quasi-periodic vortex shedding from the upstream vertical corners that resembles a von Karman street, i.e., vortices formed at each lateral side of the cube, released alternately and periodically. Also, the locus of the horseshoe vortex varies considerably in the instantaneous field [52]. It is found in [50] that the flow oscillates between roughly two states, characterized by different vortex locations, and hence the instantaneous velocity probability density function (PDF) is bimodal. This is confirmed in the LES of [52], where it is also observed that the choice of subgrid model affects the length of the recirculation zone considerably.

4.3 LES results for the surface mounted cube

We base our numerical simulation on the Martinuzzi and Tropea [50] experiment. The cube has side length H=25[mm], and the locations of measuring points are in Figure 1. The streamwise (in the mean flow direction), crosswise (normal to the bottom surface) and spanwise (parallel to the bottom surface, perpendicular to the main flow direction) coordinates are denoted x, y, z, and the corresponding velocity components are denoted u, v, w.

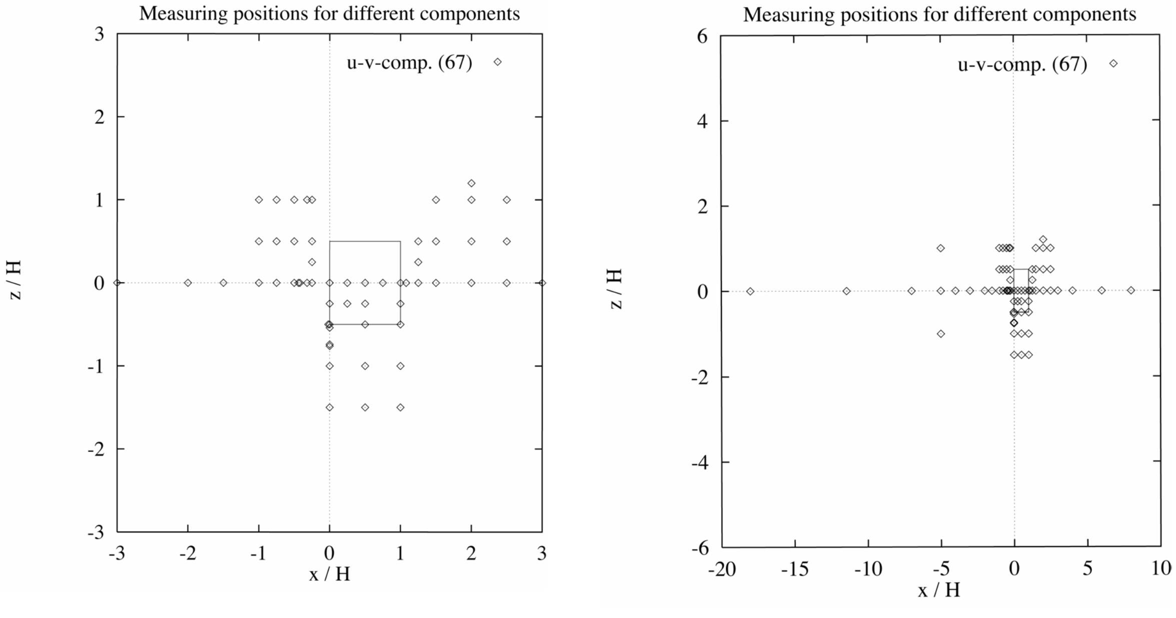

(a) (b)

Figure 6. Measurement points a) close to the cube and b) over the whole domain. Figures 6 a and b are from the Martinuzzi and Tropea dataset, reproduced by permission. At each point a vertical profile consisting of about 30 points is measured. The mean flow direction is in the direction of the x-axis.

We choose the same computational domain as in [52] and [53], namely $-3 < x < 7$, $0<y<2$, $-3<z<3$. Two grids are used, a coarse grid with 83x31x57 cells on the boundary, and a fine grid with 100x38x71 cells on the boundary. The total number of cells in the coarse grid is 154809 and in the fine grid 285050.

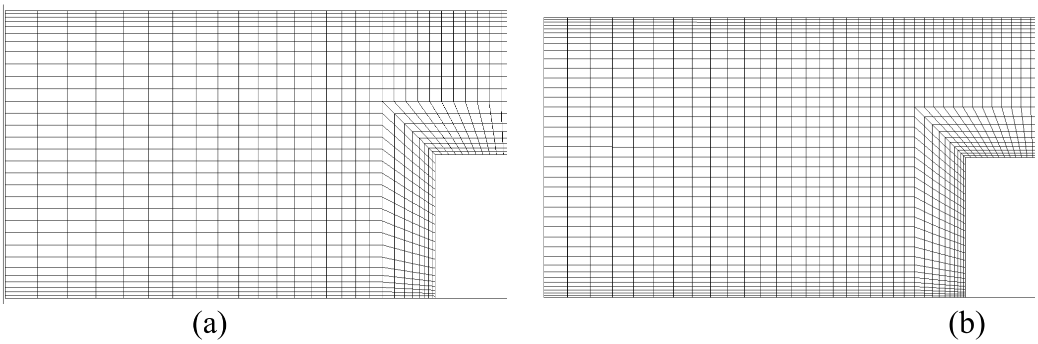
(a) (b)

Figure 7. a. The computational mesh in streamwise view (a) coarse mesh and (b) fine mesh. We see the left half of the cross-section of the mesh, viewed in the downstream direction. The mesh is generated from a number of blocks, where in each block the number of cells in each direction is specified as well as a *clustering factor*, the ratio between the thickness of the last and the first cell in each direction of the block. Close to walls, the cells are clustered towards the walls, to capture the boundary layer.

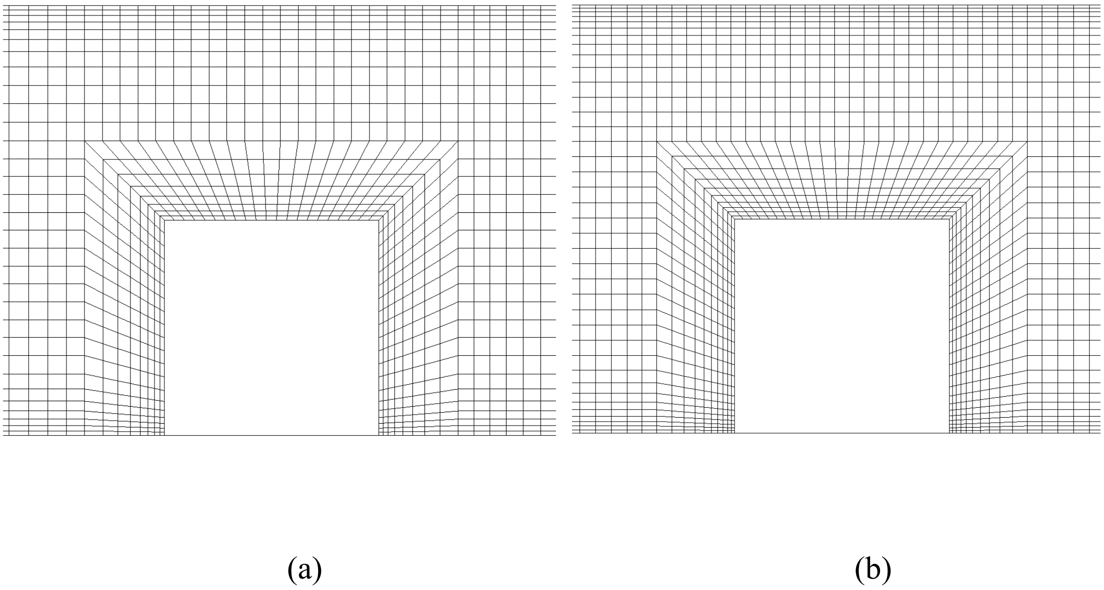
(a) (b)

Figure 8. a. The computational mesh in spanwise view (a) coarse mesh and (b) fine mesh. Here, we see the mesh cross-section with the center plane, seen from the left side of the channel. Cells are clustered towards walls the same way as in the streamwise cross-section seen in Figure 7.

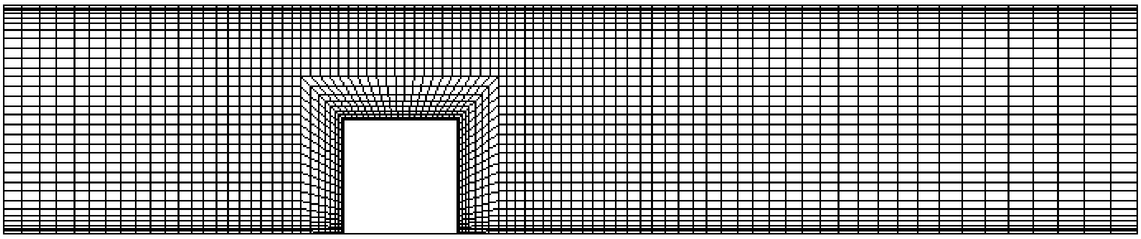

Figure 9. Coarse mesh, spanwise view. Here we see the centerplane cross-section of the mesh over the entire computational domain. Note the slight stretching of the cells towards the inlet (left) and the outlet (right).

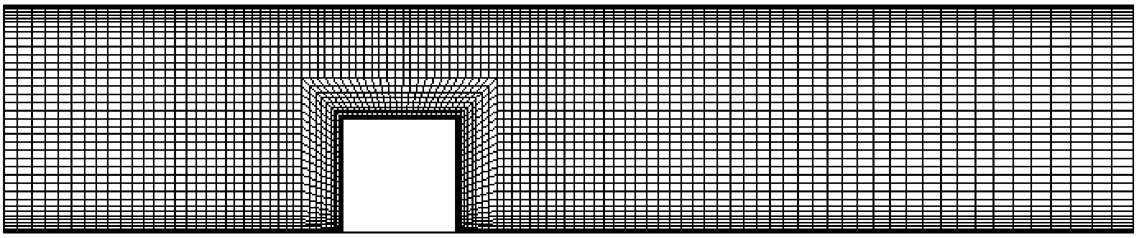

Figure 10. Fine mesh, spanwise view. Similar as Figure 9, for the fine mesh.

The first model we have considered is the MILES model.
The second model is the OEEVM+WM model (4), including a ”clipping condition” ensuring that the modeled turbulent kinetic energy $k > 10^{-10}$. Hence we have an *obstacle problem* for the modeled turbulent kinetic energy *k,* cf. [55].
We use the same inlet boundary condition as [53], namely a specified constant velocity profile (mean profile from [50]), corresponding to the mean profile of fully developed turbulent channel flow. Normal derivative of *p* is zero (Neumann boundary condition), and the modeled turbulent kinetic energy *k* is zero (Dirichlet boundary condition). In contrast, [52] use data from a turbulent channel flow simulation. For the outlet we have Neumann condition for *U*, *k*, Dirichlet condition for p, and, finally, at walls we impose no-slip condition on *U*, *p,* i.e., Dirichlet condition on *U*, Neumann condition on *p,* and for *k* we impose Neumann condition.

The results below indicate that we are able to reproduce the main features of the flow.

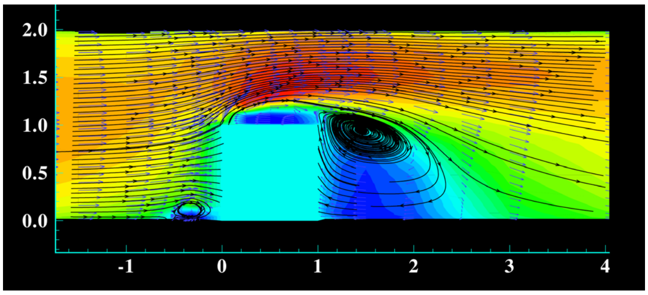

Figure 11. Average flow streamlines from the experiment by Martinuzzi and Tropea, (1993).

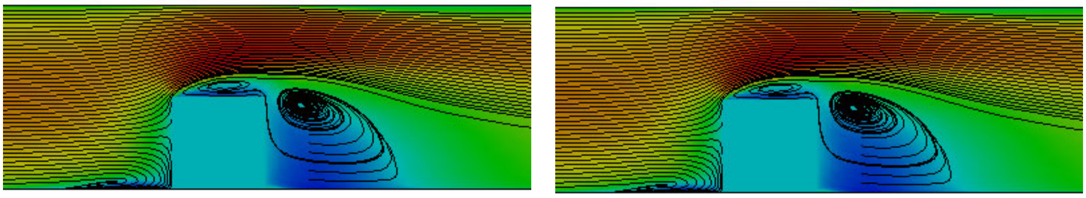

(a) (b)

Figure 12. MILES with wall model, a), coarse grid, b), fine grid. Blue signifies regions with low velocity, red signifies regions with high velocity. We see a similar streamline pattern for both grids. We also see good agreement with the streamline pattern of the experiment (figure 11) except for the location and form of the horseshoe vortex in front of the cube, which in the simulation is located too far upstream and more stretched in the flow direction, compared to the experiment (Figure 11).

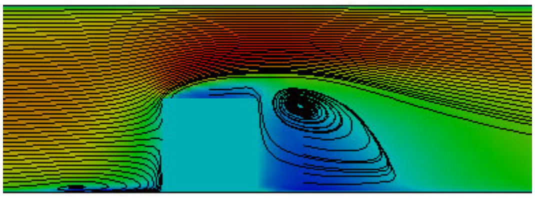

Figure 13. OEEVM with wall model, coarse grid. The only visible differences compared to the MILES model is a somewhat higher separation line from the leading edge of the cube and an even more upstream position of the center of the horseshoe vortex.

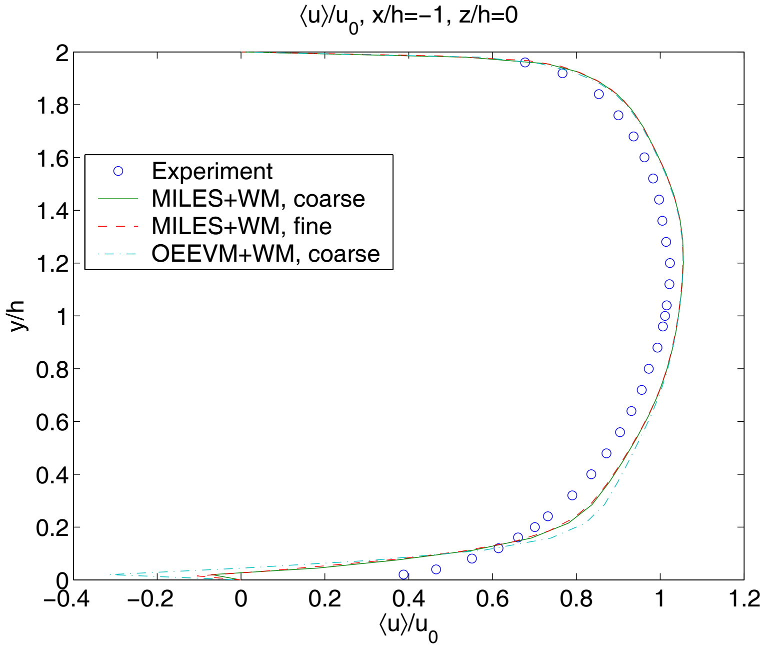

Fig. 14a. Mean streamwise velocity component at x/h=-1, y/h=0, one cube length upstream from the front face of the cube. We see excellent agreement between MILES on the coarse and fine grid (except close to the bottom), indicating that the influence of the MILES subgrid model is small in this region. The horseshoe vortex (negative velocities near the bottom) is seen in the simulations, but not in the experiment. This effect is even more accentuated for the OEEVM model. Outside the horseshoe vortex region, the mean velocity is somewhat overestimated in the simulations.

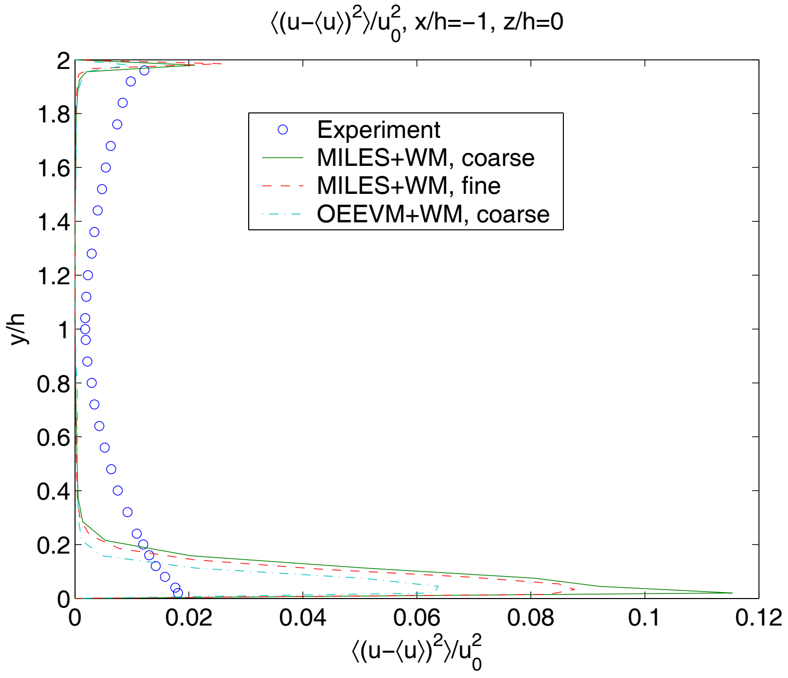

Figure 14b. Variance of the streamwise velocity component at x/h=-1, z/h=0, one cube-length upstream from the front face of the cube. The simulations overestimate the turbulence close to the walls, and underestimate the turbulence in the interior of the domain. The turbulence level is smaller for the OEEVM model.

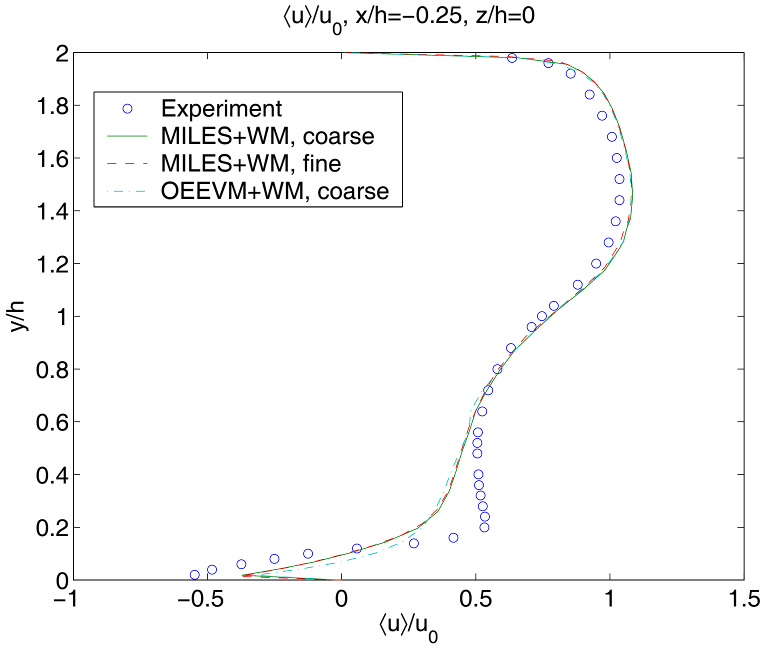

Figure 14 c. Average streamwise velocity component at x/h=-0.25, z/h=0, one quarter of a cube length upstream from the front face of the cube. Excellent agreement between all models and experiment for y/h>0.8. Experiment shows a distinct boundary for the horseshoe vortex. The horseshoe vortex formation in the simulations are smoother, and the strength of the horseshoe vortex is somewhat underestimated.

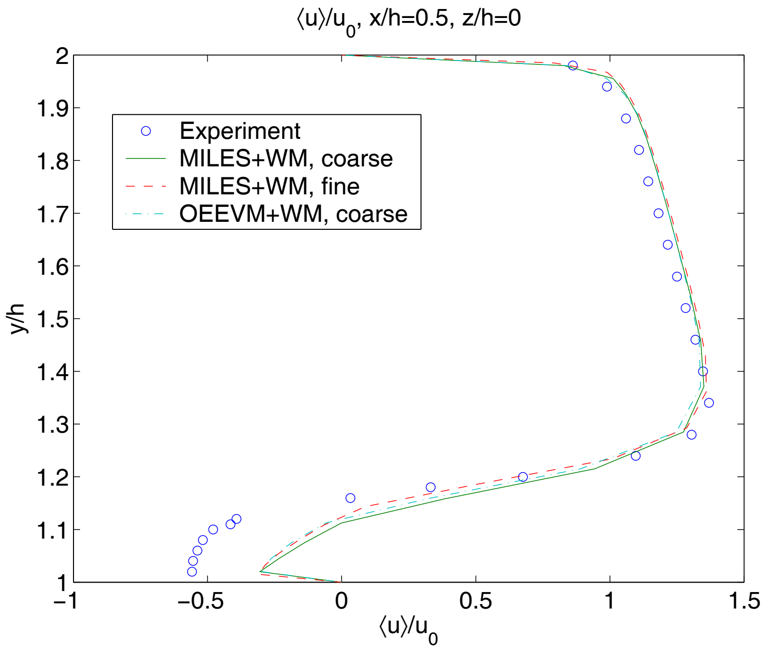

Figure 14 d. Mean streamwise velocity component at x/h=0.5, z/h=0, at the midpoint on top of the cube. The roof vortex (negative velocities) close to the roof (y/h=1) is clearly seen in the experiment, and underestimated in the simulations. Good agreement between simulations, indicating that most of the turbulence is resolved (i.e., the influence of the subgrid model is small), and hence that discrepancies between simulations and experiment is due to upstream conditions.

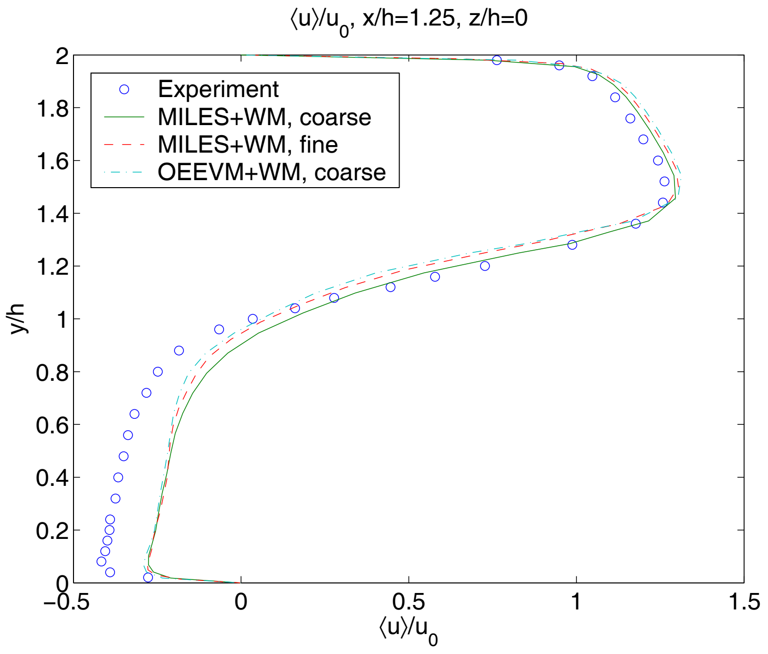

Figure 14 e. Mean streamwise velocity component at x/h=1.25, z/h=0, one quarter of a cube length downstream from the back face of the cube, in the wake region. The wake vortex region (negative velocitities) is clearly seen both in experiment and simulations. The strength of the wake vortex is underestimated in all simulations.

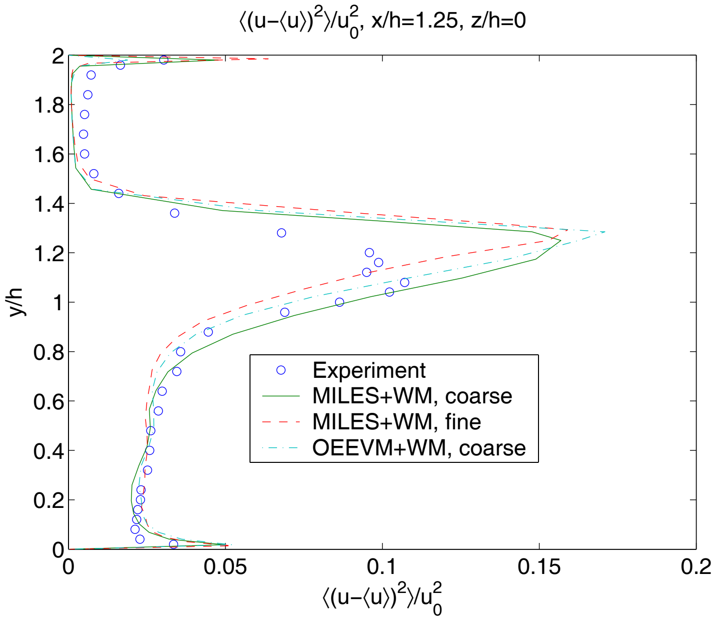

Figure 14 f. Variance of the streamwise velocity component at x/h=1.25, z/h=0, one quarter of a cube length downstream from the back face of the cube. Comparatively better agreement between simulations and experiments, compared to the upstream profile (Figure 14 b). Peaks in the variance are seen close to the bottom (y/h=0) and top (y/h=2), as well as close to the roof of the cube (y/h=1), where the largest variance is found, due to the turbulence generated by the leading edge of the top of the cube. We also see a larger amount of variance for 0<y/h<1, due to turbulence generated by the leading vertical edges of the cube.

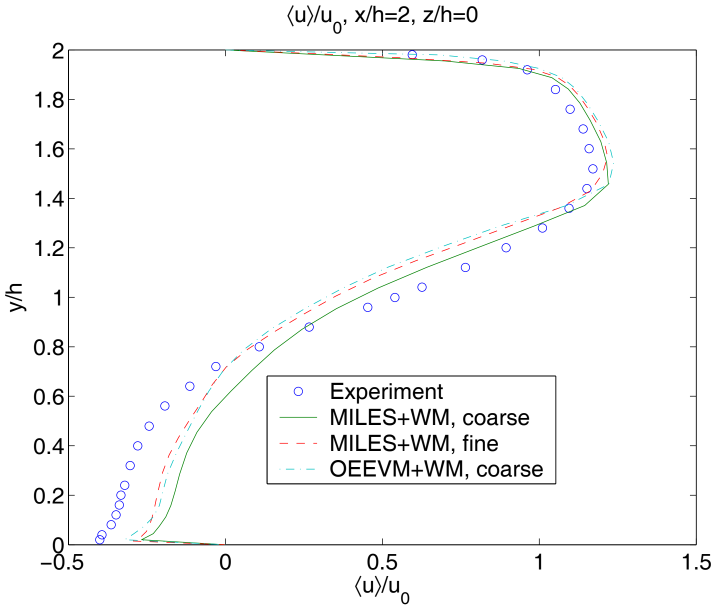

Figure 14 g. Mean streamwise velocity component at x/h=2, y/h=0, two cube lengths downstream from the back face of the cube in the wake region. The wake vortex region (negative velocitities) is clearly seen both in experiment and simulations. The strength of the wake vortex is underestimated in all simulations

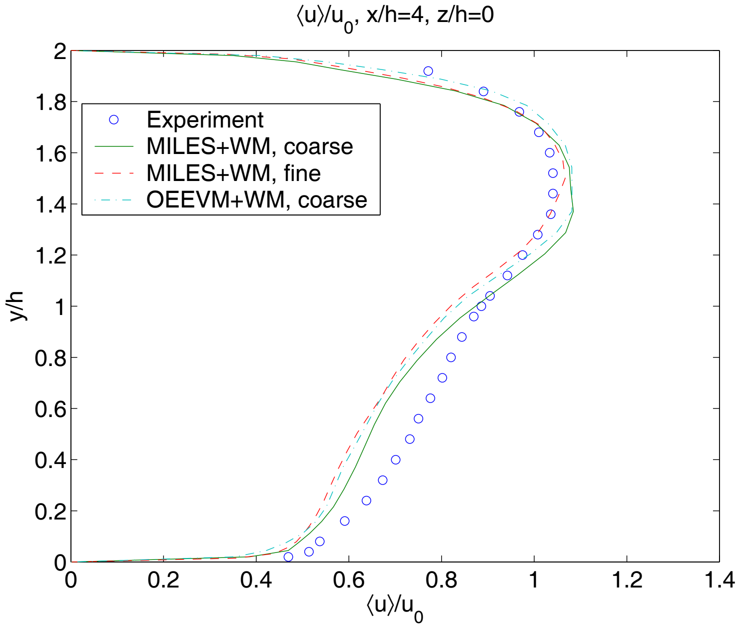

Figure 14 h. Mean streamwise velocity component at x/h=4, y/h=0, four cubelengths downstream from the back face of the cube, downstream from the wake region. No wake vortex region is visible in the mean field (mean velocities are positive).

4.4 Conclusions

As can be seen in Figures 12 to 14, we are able to reproduce the main features of the average flow, with the present grids and models. However, for second order statistical moments, our results deviate considerably from experimental results. More effort must be put into reproducing the correct flow conditions upstream from the cube. The mean flow close to the cube is rather insensitive to the choice of subgrid model on the present grids, suggesting that most of the turbulent kinetic energy is present on the resolved scales.

4.5 Suggestions for further work

To achieve correct inlet boundary conditions on the present domain, we may considerably extend the domain upstream to obtain a LES for a fully developed channel flow in the upstream part of the domain. This approach is used e.g., in [52]. We have such simulations on a prolonged computational domain in progress, but preliminary results indicates no significant differences on the results close to the cube, and downstream from the cube. Rather, the velocity profiles a few cube lengths upstream from the cube deviates more from the experimental profiles, suggesting that more work has to be done to achieve the correct upstream conditions.

On non-orthogonal meshes, the FOAM algorithm used here is not strictly of second order, because a first order skewness error is introduced on each non-orthogonal cell. This error corresponds to a diffusion term, cf. [54], p. 124. The size of the skewness error on the cube mesh should be investigated. The skewness error term can in principle be implemented in FOAM by a deferred correction approach, thereby giving a second order algorithm also on non-orthogonal meshes.

At the moment it seems unclear to what extent the sample averages have converged in the statistical sampling phase of the LES, since some of them are very irregular. We should develop FOAM tools to address this problem.

Considering Figures 15 (a) and (b) the flow pattern clearly differ considerably from the mean flow pattern. Se also Figure 16. Simulation of dispersion with LES should be tested and evaluated with dispersion experiments.

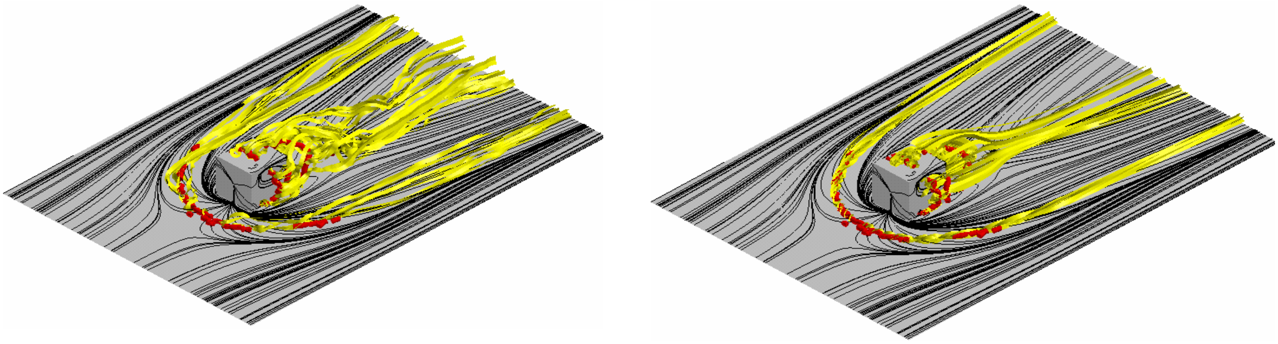

(a) (b)

Figure 15. Streamlines of (a) instantaneous velocity field and (b) time-averaged velocity field. The streamlines in the time-averaged velocity field is smoother.

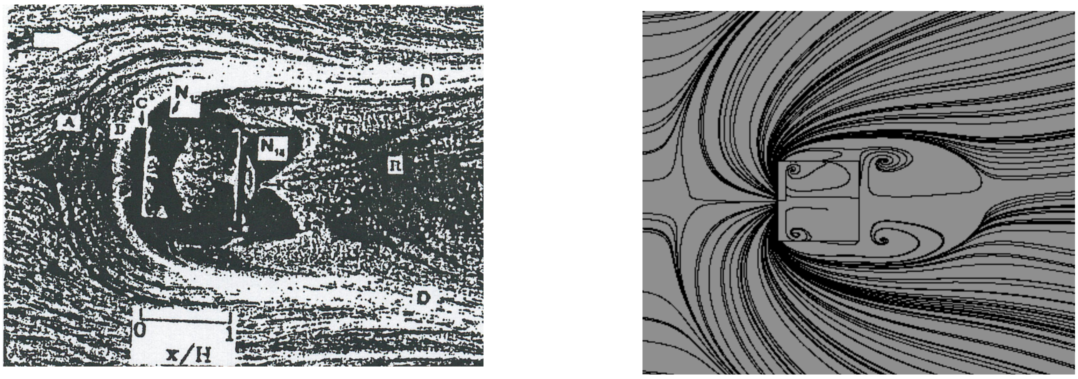

(a) (b)

Figure 16. Surface streamlines in (a) experiment (Martinuzzi and Tropea, 1993) and (b) in OEEVM with wall model, fine grid. We see a clear discrepancy in the surface streamline patterns of the simulation and the experiment. The influence region of the cube in the surface streamline pattern is much larger in the simulation compared to the experiment.

5. Flow Simulation in Urban Environment

5.1 Background

Dispersion of hazardous gases and other contaminants in urban environments is of interest. Gases and contaminants can be released through actions of terrorism or accidents and be dispersed by the wind. The large scale and complexity of the urban geometries cf. Figures 17 and 18, in combination with the large-scale flow field of the weather induced winds give a very complex flow field in an urban environment. The wind can vary both in direction and velocity in a way that is hard to predict by intuition. This can transport the contaminants in other directions and over other distances than in a more homogenous and open landscape. Therefore, it is important to be able to compute how dispersed matter is spread by the wind to be able to make an accurate decision of the hazard range, develop action plans and also to plan evacuation routes. Modern computational fluid dynamics (CFD) tools in combination with modern computers will hopefully make it possible to predict the flow field in a part of a town with reasonable accuracy. Here, the flow field in the Old Town of Stockholm has been simulated for a westerly wind of 2 m/s at 10 metres above the surface with a logarithmic profile, to demonstrate the potential in using CFD for prediction of dispersions in urban environments.

Figure 17, View over the Old Town with the royal palace at the right end of the figure, from Skeppsholmen at the eastern end of the computational domain. Photo: Urban Svennberg.

Figure 18. View over the parliament, Royal Palace, Riddarholmen and the northern part of the old town, From the City Hall (Stadshuset) at the north-west corner of the computational domain. Photo: Urban Svennberg.

5.2 Grid generation

The Old Town of Stockholm is chosen since it is a well known and central part of Stockholm, the capital city of Sweden, it contains the royal palace, the parliament and a number of governmental buildings.

Further more, it has natural limits since it is located on a few islands, the inflow and outflow boundaries for westerly wind is located over large water areas, the Riddarfjärden and Strömmen at least if the island Skeppsholmen is ignored at the outflow boundary. The location of these boundaries over water simplifies the boundary conditions. The location and size of the computational domain is plotted as a red rectangle in the map in Figure 19a, the corresponding computational domain is plotted in Figure 19b.

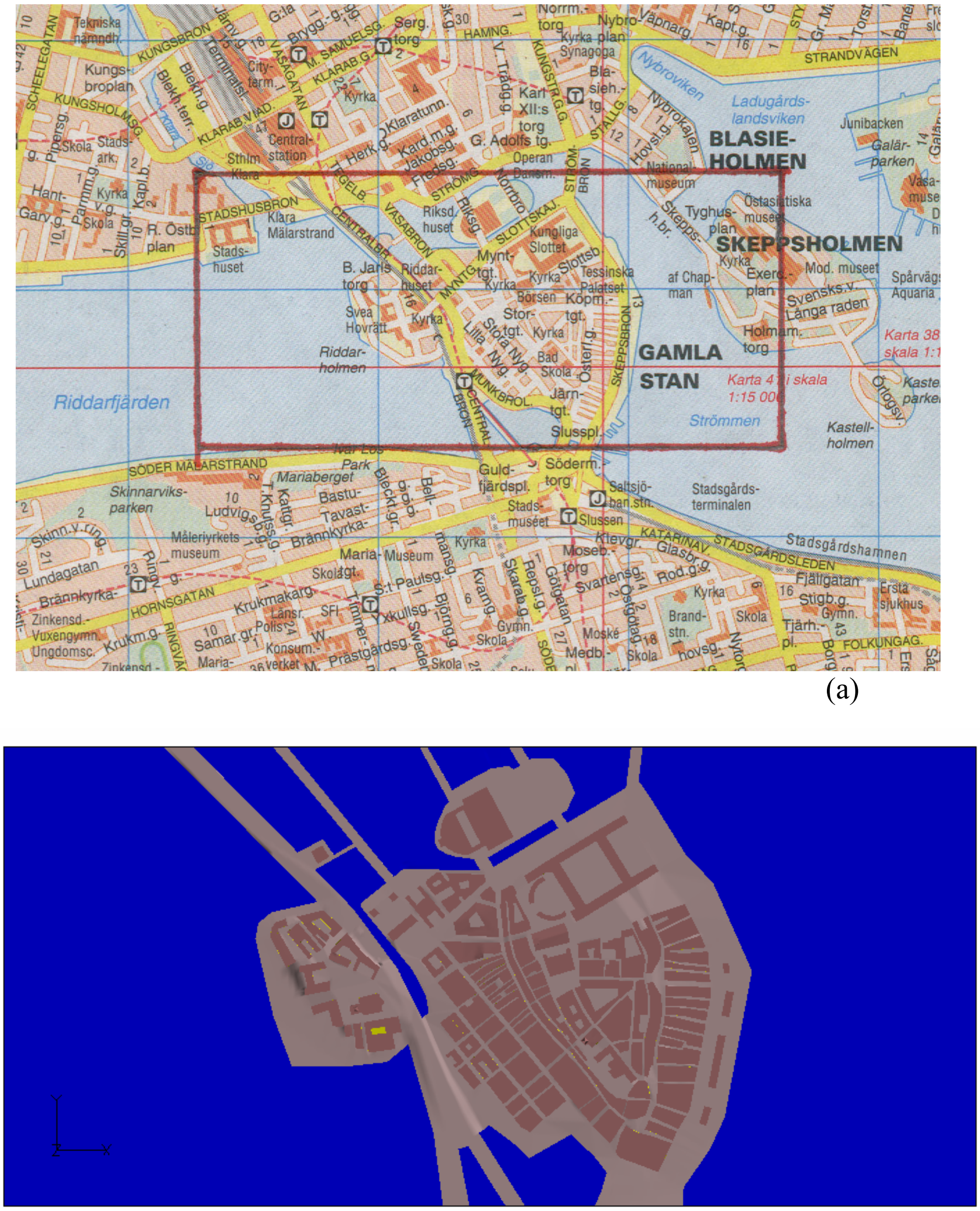

(a)

(b)

Figure 19, a: Map over central Stockholm with the computational domain marked with a red box, b: The computational domain with the simplified geometry

The buildings are built during a period of more than 400 years giving a mixture of architectural ideas, forms and sizes of the buildings and the streets and passages between them. Both narrow (approx 1.5 m) passages and wide streets are present, both straight streets with equally sized buildings in and squared pattern and curved streets with irregular formed houses complicates the geometry. This geometry has to be simplified to make it possible to generate a grid of good quality to perform the computations. Houses that are connected to each other have been considered as blocks, all roofs are flat (which they certainly not are in the real world) with a height equal to a estimated effective averaged height for the block, blocks with significantly differences in height have higher and lower parts but still with flat roofs on each part, no trees, cars or moored ships are included, most of the bridges are simplified or ignored, a few streets/passages have been ignored, a few vertical slopes of the ground have been replaced with steep slopes, and the houses at the north side of the domain have also been ignored. Windows and all other small details of the houses have been ignored since the resolution possible to achieve is not sufficient to resolve those. A few cylindrical parts of buildings and backyards are replaced with square ones for the same reason. The number of buildings/blocks have in this way been reduced too approximately 110.

The size of the computational domain is 1 750 x 830 x 1000 m in the streamwise, crosswise and vertical directions respectively. If the number of computational cells are limited to 4 000 000, the average side of the cells would be 3.3 m. The cells are clustered around the buildings so that the narrowest passage between houses/blocks at least has three cells across. This makes the largest cells in the air volume above the town considerably larger. The computation described here is made using 1 622 897 cells, a finer computation, using 4 123 160 cells, is planed for to quantify the numerical errors, most of the refinement is made in the vicinity of the houses. This grid is also smoother than the coarse one.

The inflow boundary supplied a log-linear velocity profile with a wind speed of 2 m/s at 10 meters height. The utflow uses transmissive boundary conditions for the flow to be able to pass through, while the lateral and upper boundaries use a symmetry plane boundary condition.

No-slip conditions are applied at the water surface, the ground and the house roofs, while slip condition is applied at the house walls and the side and top boundary of the bounding box. The house walls should be considered as no-slip walls to be physically correct but that would require a considerably higher number of cells to resolve the boundary layer here. The lack of resolution would result in to high a blockage ratio in the narrow streets and passages, reducing the flow in an unphysical way. Therefore, slip condition has been chosen to get a more realistic flow.

The computational grid is a structured grid made with hexahedral elements. A structured grid built with hexahedral elements have numerical advantages over unstructured grids based on tetrahedral elements, the disadvantage is that it is much more complicated to generate a structured grid for complex geometries. Most of the houses can be considered as squared blocks and therefore simple to grid by a structured hexahedral mesh. But since a large part of the old town is old it has a variety of geometries. After simplification we have a few blocks of polygonal form with almost triangular shape. These blocks concentrates the gridlines in the structured mesh giving undesirable high concentrations of grid lines in some areas. A few buildings with circular arcs give quite skewed cells. The western part of the old town has a nice almost Cartesian topology but it is not aligned with the main flow direction. The eastern most line of buildings also has a rectangular topology but slightly curved. The north end of this line is parallel to the western part of the old town while the south end of this row meets the western blocks under almost 90 degrees angle. Since it is a structured grid these gridlines have to stay parallel all the way giving high concentration of cells at the southern end of the old town and also an area with highly skewed cells. Here, four blocks have been replaced with one continuous block to reduce skewness. A computational grid of good quality should be as orthogonal as possible and have smooth transitions between areas of different grid densities. The geometry of the old town makes it impossible to achieve that everywhere. This coarse grid was completed to make sure that the skewness not was too severe and that the sudden changes in resolution in some areas were not to severe for the solver to give a solution. A few adjustments had to be done before the code ran swiftly. The results computed on this coarse grid will be used both for comparison with the results on the finer grid and as a starting solution for the finer grid.

5.3 Solver

The size and complexity of city geometry gives a very wide band of scales that are of importance for the flow field. It is prohibitively expensive to resolve all of them already for one building. The fact that we have more than 100 buildings does not make it easier. LES reduces the need for resolution but still, it is prohibitively expensive to have a resolution fine enough for to scientifically guarantee an accurate and reliable result. RANS or even potential flow methods reduce the need for resolution to a more satisfactory level but we would only get the time averaged flow field. The large-scale fluctuations, that RANS do not capture, in the vortex and recirculation structures are responsible for much of the transport of the contaminants. Still, this coarse grid, that we can afford, in combination with MILES do capture many large-scale time dependent phenomenon that are of importance for the dispersion of contaminants. There are no full-scale measurements to use as reference. Therefore, this computation is only a demonstration of what will be possible with more computational resources. There is a need for a series of computations and experiments on simpler cases ranging from a single cube mounted on a flat surface through a number of cubes in different configurations all the way to city like geometries to be able to validate computations like this one in the Old town, presented here.

5.4 Results and discussion

The computations reveal a very complex flow field containing many interesting flow structures such as large vortices behind buildings like the royal palace and the parliament buildings. These results are for the instantaneous velocity field. The computations have not been run for long enough time to reach a statistically converged state, where the time averaged velocity field is reliable. Backflow is found both behind and in front of buildings with walls perpendicular to the westerly wind. One example of this is the royal palace in Figure 20, where the wind 2m above the ground is plotted as velocity vectors coloured by the magnitude of the flow velocity, where red represent 1.5 m/s and blue 0 m/s. The main winddirection is in the positive x direction while the wind mostly goes in the opposite direction in both the outer and inner courtyard of the royal palace at this level, 2m above the ground. Another example is a place called Köpmansbrinken in the eastern part of the old town, see Figure 21. Here, the approaching wind coming through the street Köpmangatan have the expected direction but the ground is going down hill here generating a recirculation zone, giving wind in the opposite direction in the other streets approaching this place.

A Karman Vortex Street can be found around the top of the German church (Tyska kyrkan) at the central part of the Old Town. The plots in Figure 22 contain the velocity profiles at 50m above the sea level that is approximately 20m above the roofs of the houses in the surrounding area. The resolution is not sufficient to get a complete vortex street but there are significant traces of it in the wake. In Figure 22a it can also be seen that there are no vortex street behind the top of the church close to the Royal Palace (Storkyrkan). This is probably due to the coarse grid resolution in this area.

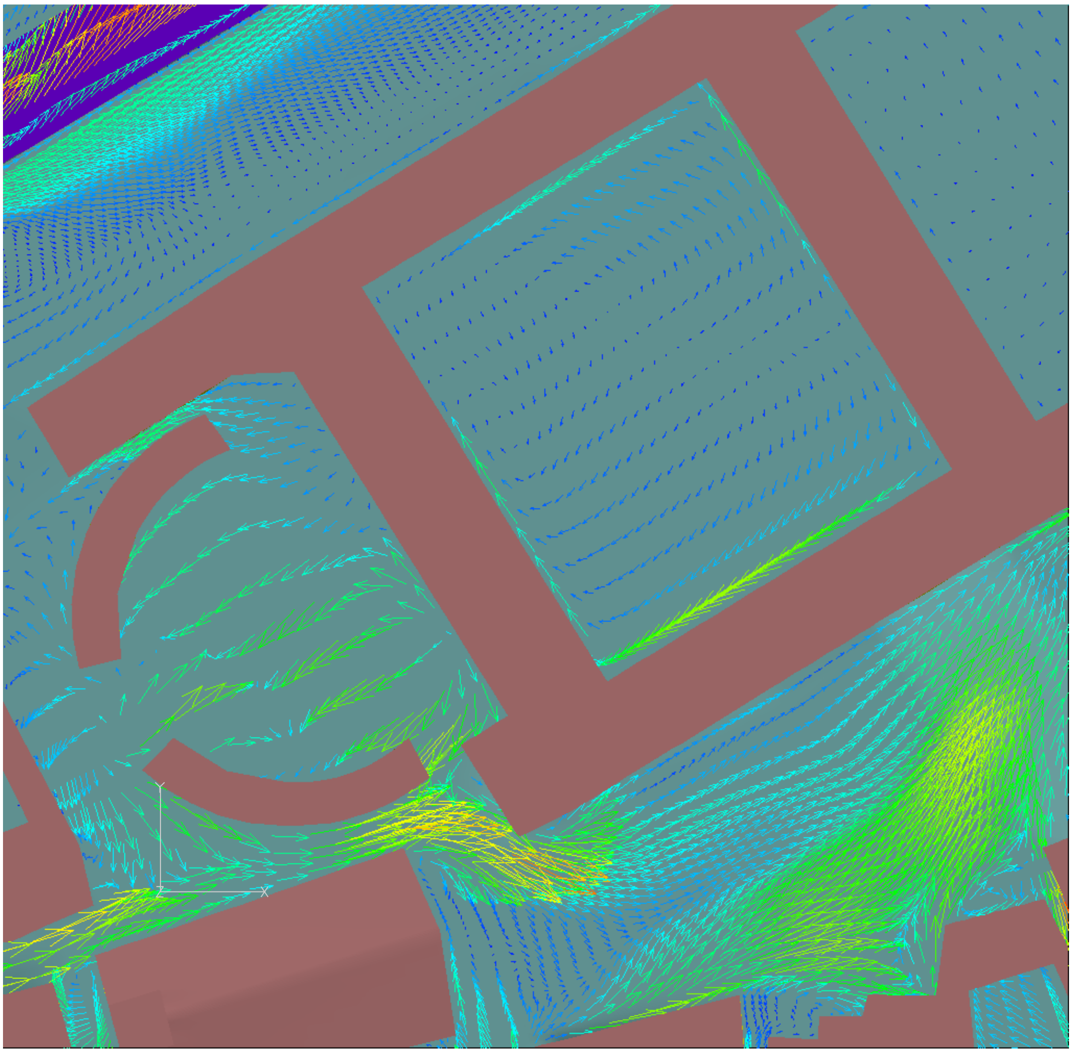

Figure 20, Wind velocity vector 2m above the ground around the royal palace.

The area behind the parliament contains a large vortex structure, see Figure 23. This area is partially covered by trees in the real world, see Figure 24. These trees will probably reduce the velocities and the rotation of the vortices here. This is an effect that is not captured since it is not straightforward to implement a correct damping function simulating the nature of a tree. A tree reduces the wind velocity but it does not stop it totally and the reduction is dependent on how many branches and leaves the tree has in different parts of it.

The old town contains many houses and around each of them there can be found interesting flow fields. The results presented here are preliminary and therefore it is pointless to and would be too lengthy to describe them all in detail, therefore, just e few examples have been chosen here. Figure 25 below, show the complex flow field through 1000 streamlines initiated at randomly chosen points at the house walls and computed in both directions in the instantaneous velocity field.

5.5 Conclusions

A computation using MILES has been performed for the flow field in the Old Town of Stockholm for a westerly wind velocity at 10 meters height of 2 m/s. The geometry has been simplified to make the computations possible. The resolution of the grid is not fine enough to capture all the details of the buildings and the effect of the simplifications is thus reduced. The instantaneous flow field is reported since the computational time is not long enough to get statistically converged results and thereby a correct average flow field. These results will be used as a starting point for the computation of dispersions both on the coarse grid reported here and a finer grid mentioned above. The results here reveal a very complex flow field in the urban environment. They also show that it is possible to compute such flow fields with large enough computers.

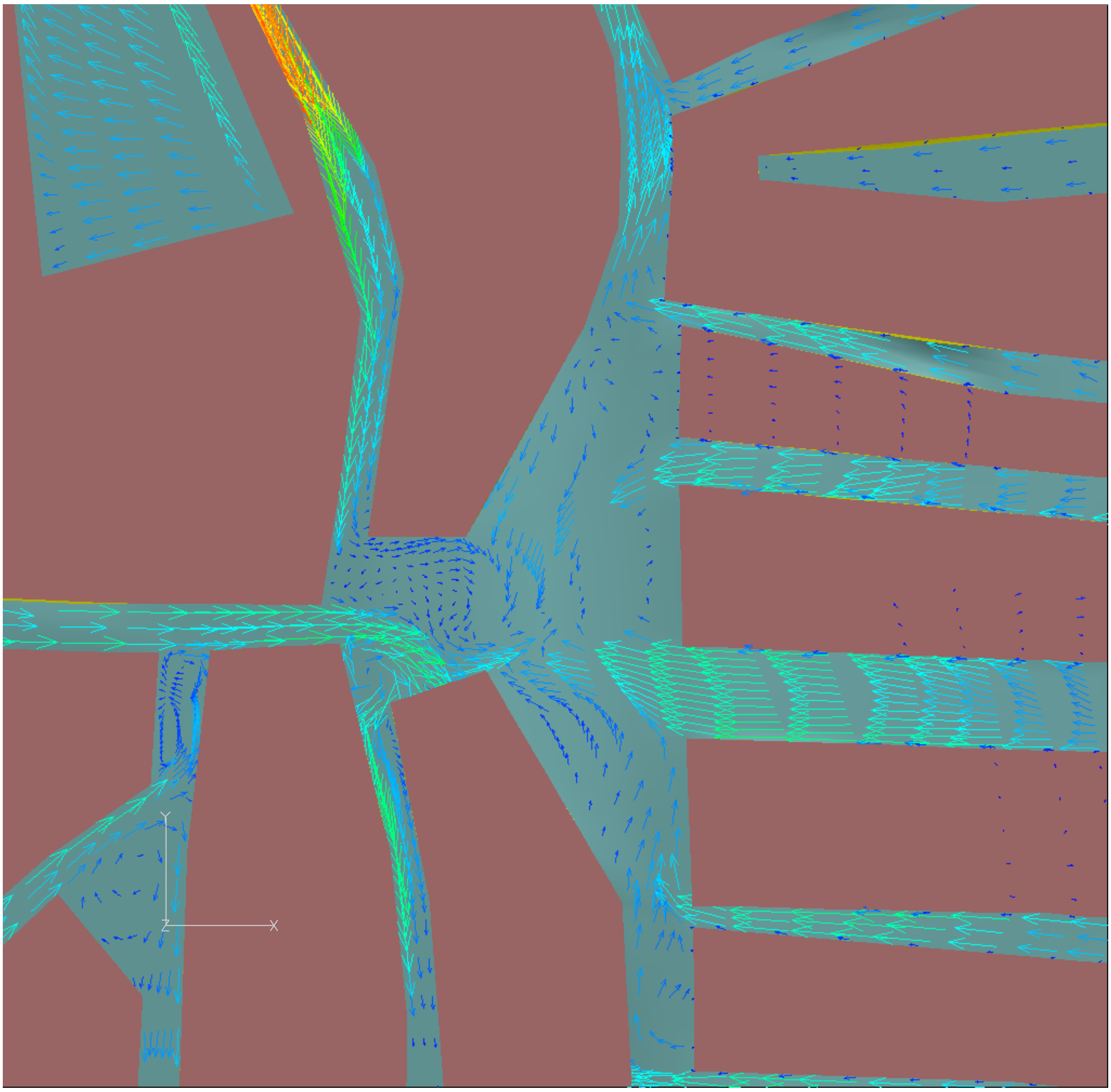

Figure 21, Wind velocity vector 2m above the ground at Köpmanbrinken in the eastern part of the old town.

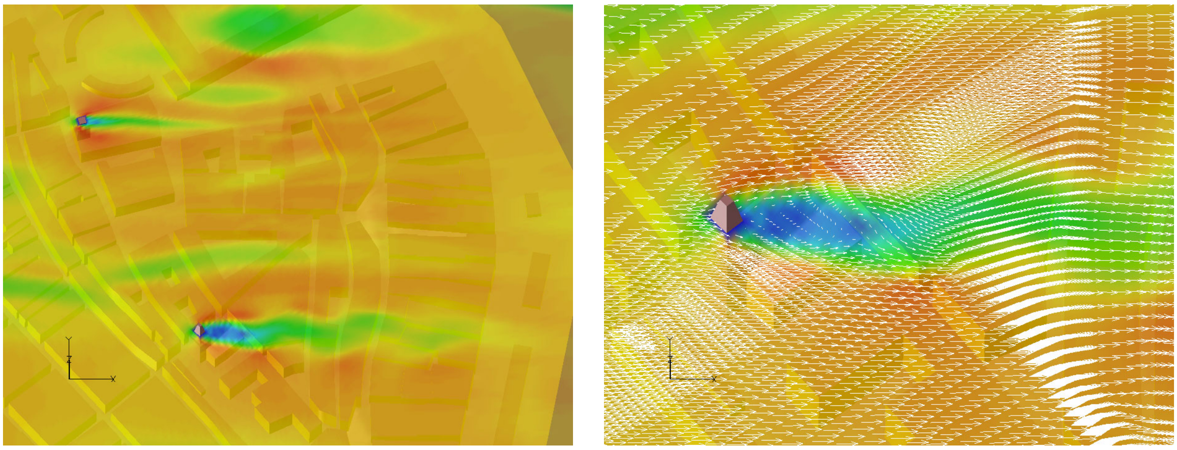

(a) (b)

Figure 22, a:Wind velocity contours at 50m above sea level, b: close up including velocity vectors at the top of the German church (Tyska kyrkan)

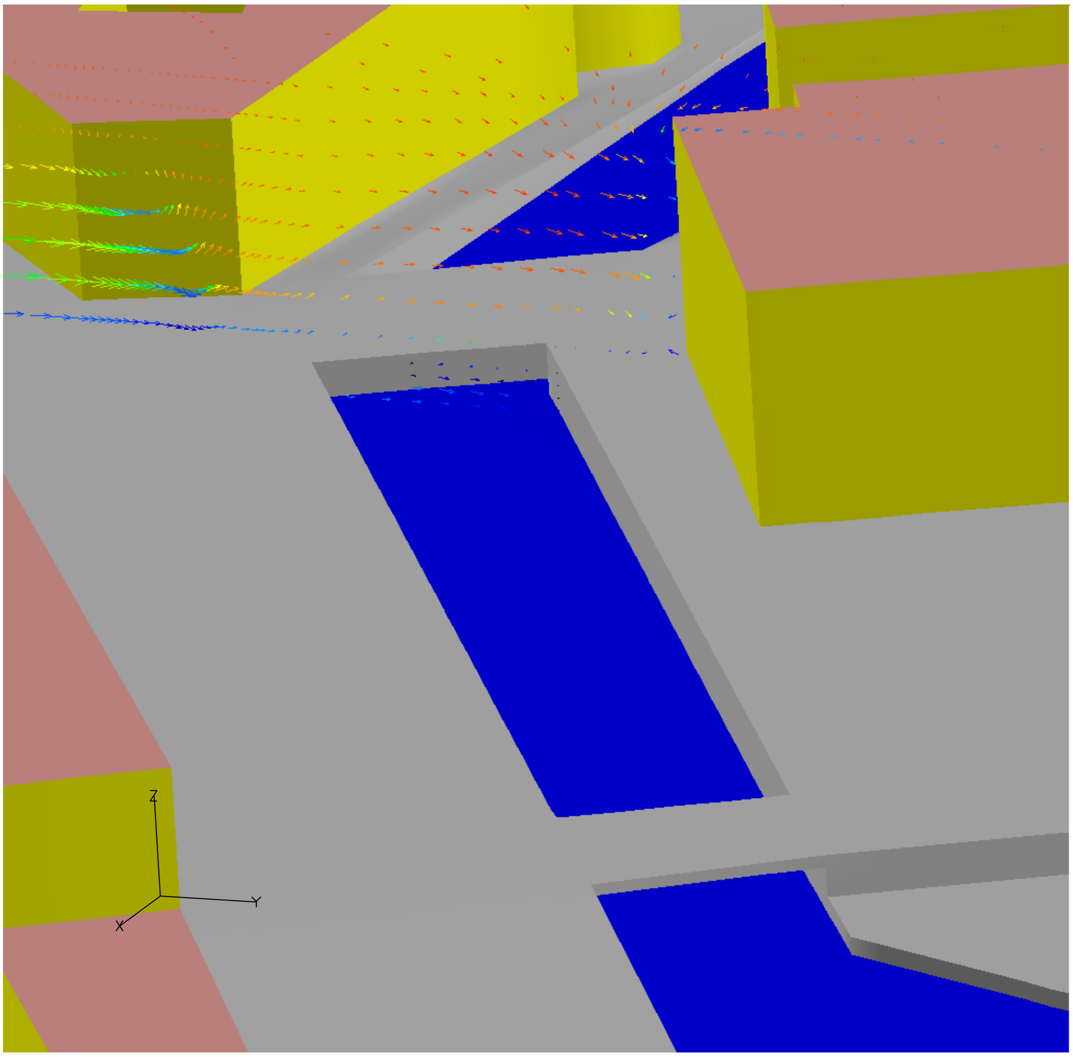

Figure 23, Velocity contours and vectors at a plane 2m above sea level and a vertical plane with constant x coordinate right behind the parliament.

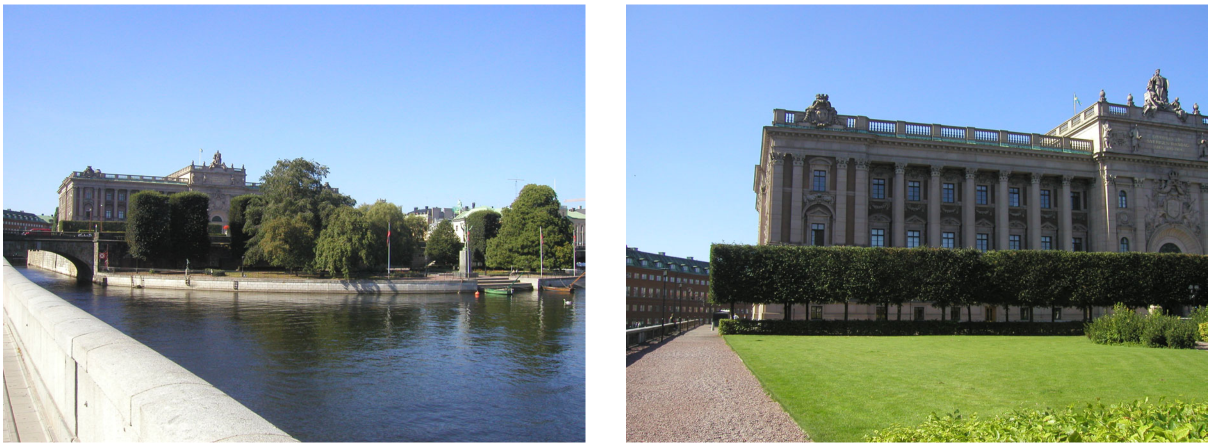

(a) (b)

Figure 24, Photos of the area behind the parliament. Photo: Urban Svennberg.

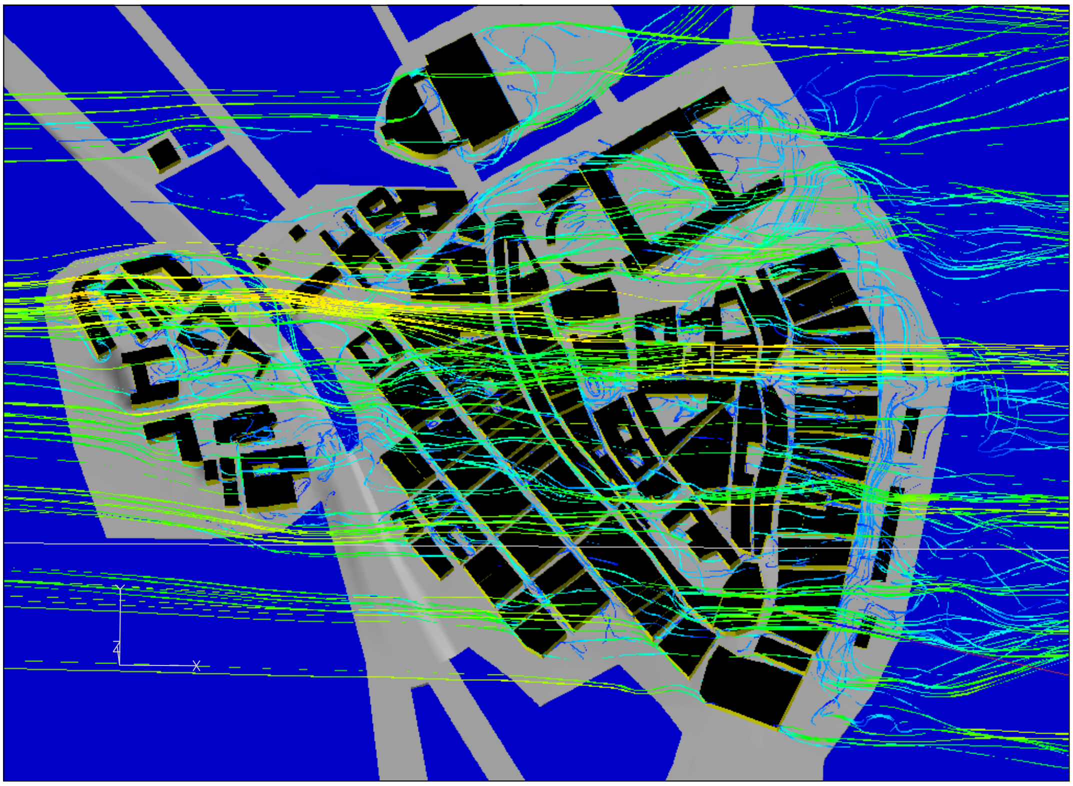

Figure 25, Streamlines initiated at 1000 randomly chosen points at the house walls and computed in both directions in the instantaneous velocity field.

6. Summary

LES can be used to simulate wind flow in an urban environment but it is shown that there are some improvements left for future work. The validation studies for the channel flow and flow around a surface mounted cube show that the mean flow is well described but the variances (<u^2>), have some discrepancy to measured values, although the result seem to be rather insensitive to the choice of sub grid models. This suggests that most of of the turbulent kinetic energy is present on the resolved scales. One of the sub grid models that showed good results in both tests was MILES and therefore it was used for the simulation of flow in Gamla Stan. A difficulty in performing a simulation of Gamla Stan was the construction of the geometry. As a hexahedral grid was used it was not possible to achieve a uniform resolution. To achieve a sufficient resolution on the lee side of a grid spreading object, like the house of parliament, an unnecessary high resolution is required on the windward side.

The computations reveal a very complex flow field containing many interesting flow structures such as the large vortices behind buildings like the royal palace and the parliament buildings. These results are for the instantaneous velocity field.

Atmospheric flow in general includes atmospheric stability which is important both for the mean flow and for dispersion. In this study a neutral stratification is assumed as a first step. Studies of atmospheric stability using LES is performed separately [56].

Dispersion will also probably be sensitive to the configuration of the buildings or other obstacles. Next step is to simulate dispersion within the flow here presented. Validation studies of dispersion simulation with LES will be performed as a next step comparing simulations with experimental data such as flows in wind tunnels, water channels etc..

7. Acknowledgements

The authors wishes to thank Per Ola Andersson and Ronny Bergman for their valuable advice on the manuscript.
The municipality of Stockholm (stadsbyggnadskontoret), has graciously supplied some of the data used for generating the geometry.

8. Abbreviations

CT	Contaminant Transport
GS	Grid Scale
SGS	Sub Grid Scale
CFD	Computational Fluid Dynamics
NSE	Navier Stokes Equations
Re	Reynolds number (=UL/ν)
DNS	Direct Numerical Simulation
RANS	Reynolds Averaged Navier Stokes
LES	Large Eddy Simulation
SMG	Smagorinsky model
DSMG	Dynamic Smagorinsky Model
OEEVM	One-Equation-Eddy-Viscosity Model
DLM	One-Equation Dynamic Localization Model
LDKM	Localized Dynamic Kinetic Energy Model
LDM	Lagrangian Dynamic
MM	Model Mixed Model
DES	Detached Eddy Simulation
DSEM	Differential Stress Equation Model
MILES	Monotone Integrated LES
FCT	Flux Corrected Transport
WM	Wall Model
FV	Finite Volume

9. References

[1] Speziale C.G.; 1996, ”Modeling of Turbulent Transport Equations”, in Simulation and Modeling of Turbulent Flows Eds. Gatski T.B., Hussaini M.Y. & Lumeley J.L. Oxford University Press, New York.
[2] Launder B.E.; 1996, “An Introduction to Single-Point Closure Methodology”, in Simulation and Modeling of Turbulent flows Eds. Gatski T.B., Hussaini M.Y. & Lumeley J.L. Oxford University Press, New York.
[3] Wilcox D.C.; 1998, ‘Turbulence Modelling for CFD”, DCW Industries.
[4] Pope S.B.; 2000, “Turbulent Flows”, Cambridge University Press.
[5] Ferziger J.H. & Leslie D.C.; 1979, “Large Eddy Simulation – A Predictive Approach to Turbulent Flow Computation”, AIAA paper 79-1441.
[6] Sagaut, P.: Large Eddy Simulation for Incompressible Flows, Springer Verlag, Heidelberg, 2001
[7] Fureby C.; 2001, ‘Towards Large Eddy Simulation of Complex Flows, In Direct and Large Eddy Simulation IV, Eds. Friedrich R. & Rodi W., Kluwer, The Netherlands.
[8] Lesieur M & Metais O; 1996, “New Trends in Large Eddy Simulations of Turbulence”, Annu. Rev. Fluid Mech., 28, p 45.

[9] Boris, J.P., Grinstein, F.F., Oran, E.S. & Kolbe, R.L.; 1992, ”New Insights into Large Eddy Simulation”, Fluid Dyn. Res., 10, p 199.
[10] Grinstein F.F. & Karniadakis G.E.; 2002, ”Special Section on Altemative LES and Hybrid RANS/LES for Turbulent Flows”, J. Fluids Eng., 124,p 821.
[11] Bagget J.S., Jiménez J. & Kravchenko A.G.; 1997, ”Resolution Requirements in Large Eddy Simulations of Shear Flows”, Ann. Res. Breiefs, CTR, NASA Ames/Stanford University, p 55.
[12] Ghosal, S. & Moin P.; 1995, “The Basic Equations for the Large Eddy Simulation of Turbulent Flows in Complex Geometry”, J. Comp. Phys., 118, p 24.
[13] Fureby, C. & Tabor, G.; 1997, “Mathematical and Physical Constraints on Large Eddy Simulations”, J. Theoretical Fluid Dyn., **9**, 85.

[14] Vreman B., Geurts B. & Kuerten H.; 1994, “Realizability Conditions for the Turbulent Stress Tensor in Large Eddy Simulation”, J. Fluid Mech., **278**, p 351.

[15] Speziale C.G.; 1985, “Galilean Invariance of Sub Grid Scale Stress Models in the Large Eddy Simulation of Turbulence“, J. Fluid Mech., **156**, p 55.

[16] Geurts B.J.; 2001, “Balancing Errors in LES”, In Direct and Large Eddy Simulation IV, Eds. Friedrich R. & Rodi W., Kluwer, The Netherlands.

[17] Schumann U.; 1975, “Subgrid Scale Model for Finite Difference Simulation of Turbulent Flows in Plane Channels and Annuli”, J. Comp. Phys., **18**, p 376.

[18] Smagorinsky J.; 1963, “General Circulation Experiments with the Primitive Equations. I. The Basic Experiment”, Month. Wea. Rev., **91**, p 91.

[19] Germano M., Piomelli U., Moin P. & Cabot W.H.; 1994, “A Dynamic Sub Grid Scale Eddy Viscosity Model”, Phys. Fluids A **3**, p 1760.

[20] Ghosal S., Lund T.S., Moin P. & Akselvoll K.; 1995, “A Dynamic Localization Model for Large Eddy Simulation of Turbulent Flows”, J. Fluid Mech, **286**, p 229.

[21] Kim W.-W. & Menon S.; 1994, “A New Dynamic One Equation Sub Grid Scale Model for Large Eddy Simulations”, AIAA Paper No 95-0356.

[22] Kim W.-W. & Menon S.; 1997, “Application of the Localized Dynamic Subgrid Scale Model to Turbulent Wall-Bounded Flows”, AIAA Paper No 97-0210.

[23] Kim W.-W., & Menon S.; 1999, “A new Incompressible Solver for Large-Eddy Simulations”, Int. J. Num. Fluid Mech., **31**, p 983.

[24] Meneveau C., Lund T.S. & Moin P.; 1996, “A Lagrangian Dynamic Subgrid-scale Model of Turbulence”, J. Fluid Mech., **319**, p 353.

[25] Bardina J., Ferziger J.H. & Reynolds W.C.; 1980, “Improved Subgrid Scale Models for Large Eddy Simulations”, AIAA Paper No. 80-1357.

[26] Deardorff, J.W.; 1973, “The Use of Subgrid Transport Equations in a Three-Dimensional Model of Atmospherical Turbulence”, ASME, J. Fluids Engng. Trans., **95**, 429.

[27] Carati D. & Cabot W.; 1996, “Anisotropic Eddy Viscosity Models”, Proceedings of the Summer Program – CTR, p 325.

[28] Abba A., Bucci R., Cercignani C. & Valdettaro L.; 1996, “A New Approach to the Dynamic Subgrid Scale Model”, Unpublished.

[29] Horiuti K.; 1993, “A Proper Velocity Scale for Modelling Subgrid Scale Eddy Viscosities in Large Eddy Simulation”, Phys. Fluids A, **5**, p 146.

[30] Sullivan P.P., McWilliams J.C. & Moeng C.H.; 1994, “A Subgrid Scale Model for Large Eddy Simulation of Planetary Boundary Layer Flows”, Boundary-layer Meteorol., **71**, p 247.

[31] Voke, P.; 1996, “Subgrid-scale Modeling at Low Mesh Reynolds Number”, J. Theoretical Fluid Dyn., **8**, p 131.

[32] Wang M.; 1997, “Progress in Large Eddy Simulation of Trailing Edge Turbulence and

Aeroacoustics", Annual Research Briefs – CTR, p 37.

[33] Wang M. & Moin P.; 2001, "Wall Modelling in LES of Trailing Edge Flow", Turbulence and Shear Flow Phenomena, Vol II, Eds. Lindborg E. *et al.*, p 165.

[34] Spalart P.R., Jou W.-H., Strelets M. & Allmaras S.R.; 1997, "Comments on the Feasibility of LES for wings, and on a Hybrid RANS/LES Approach", Advances in DNS/LES, 1st AFSOR Int. Conf. On DNS/LES, Greyden Press, Columbus Oh.

[35] Boris J.P. & Book D.L.; 1973, "Flux Corrected Transport I, SHASTA, a Fluid Transport Algorithm that Works", J. Comp. Phys. **11**, p 38.

[36] Garnier E., Mossi M., Sagaut P., Comte P., & Deville M.; 2000, "On the Use of Shock-Capturing Schemes for Large Eddy Simulation", J. Comp. Phys., **153**, p. 273.

[37] Okong'o N., Knight D.D., & Zhou G.; 2000, "Large Eddy Simulations Using an Unstructured Grid Compressible Navier-Stokes Algorithm", Int. J. Comp. Fluid Dynamics **13**, p. 303.

[38] Margolin L.G., Smolarkiewicz P.K., & Sorbjan Z.; 1999, "Large-Eddy Simulation of Convective Boundary Layers Using Non-Oscillatory Differencing", Physica D, **133**, p 390.

[39] Karamanos G.-S. & Karniadakis G.E.; 2000, "A Spectral Vanishing Viscosity Method for Large-Eddy Simulations", J. Comp. Phys., **163**, p 22.

[40] Fureby C. & Grinstein F.F.; 2002 "Large Eddy Simulation of High Reynolds Number Free and Wall Bounded Flows", J. Comp. Phys., **181**, p 68.

[41] Grinstein F.F. & Fureby C.; 2002, "Recent Progress on MILES for High Re Flows", J. Fluids Engng., **124**, p 848.

[42] Hirsch C.; 1999, "Numerical Computation of Internal and External Flows", J. Wiley & Sones.

[43] Sandham N.D. & Howard R.J.A.; 1995, "Statistics Databases from Direct Numerical Simulation of Fully-Developed Turbulent Channel Flow", Private communication, QMW-EP-1106, Queen Mary & Westfield College, Department of Engineering. London, UK.
[44] Antonia R.A., Teitel M., Kim J., & Browne L.W.B.; 1992, "Low-Reynolds-Number Effects in a Fully Developed Turbulent Channel Flow", J. Fluid Mech. 236, p 579.
[45] Wei T. & Willmarth W.W.; 1989, "Reynolds Number Effects on the Structure of a Turbulent Channel Flow", J. Fluid Mech. 204, p 57.
[46] Dean R.B.; 1978, "Reynolds Number Dependence of Skin Friction and other Bulk Flow Variables in Two-Dimensional Rectangular Duct Flow", Trans. ASME I: J. Fluids Eng., 100, p 215.
[47] Sandham N.D. Howard R.J.A.;1995, "Statistics of Fully-Developed Turbulent Channel Flow",Private Communication QMW-EP-1106,Queen Mary &Westfield College, Department of Engineering. London U.K.
[48] Castro I. P. and Robins A. G., The flow around a surface-mounted cube in uniform and turbulent streams. J. Fluid Mech. 79 (1997) 2, pp. 307-335.
[49] Hunt J. C. R., Abell C. J., Peterka J. A. and Woo H., Kinematical studies of the flows around surface-mounted obstacles; applying topology to flow visualization. J. Fluid Mech. 86 (1978), pp. 179-200.
[50] Martinuzzi R. and Tropea C., The flow around surface-mounted, prismatic obstacles placed in a fully developed channel flow. J. Fluids Eng. 115 (1993), pp. 85-91.
[51] Larousse, A., Martinuzzi, R. and Tropea, C. (1991) Flow around Surface-Mounted, Three-Dimensional Obstacles, 8th Symposium on Turbulent Shear Flows, TU-Munich/German, 1, pp. 14-4-1/14-4-6.
[52] Shah K. B. and Ferziger J. H., A fluid mechanichians view of wind engineering: Large eddy simulation of flow past a cubic obstacle. J. Wind Eng. and Ind. Aerodyn. 67&68 (1997), pp. 211-224.
[53] Krajnovic S. and Davidson L., Large-Eddy Simulatio of the Flow Around a Bluff Body, AIAA Journal (40) no. 5, 2002, pp. 927-936.

[54] Jasak H., Error Analysis and Estimation for the Finite Volume Method with Applications to Fluid Flows, Doctoral Thesis, Department of Mechanical Engineering, Imperial College, London, 1996.
[55] Friedman A., Variational Principles and Free-Boundary Problems,
Wiley, 1982.
[56] von Schoenberg P. master thesis, Stockholm University, 1999.